Long bone shape variation in the forelimb of Rhinocerotoidea: relation with size, body mass and body proportions

Christophe Mallet, Alexandra Houssaye, Raphaël Cornette, Guillaume Billet

▶ **To cite this version:**

Christophe Mallet, Alexandra Houssaye, Raphaël Cornette, Guillaume Billet. Long bone shape variation in the forelimb of Rhinocerotoidea: relation with size, body mass and body proportions. Zoological Journal of the Linnean Society, inPress, 10.1093/zoolinnean/zlab095 . hal-03611154

HAL Id: hal-03611154
https://hal.science/hal-03611154

Submitted on 8 Jun 2022

HAL is a multi-disciplinary open access archive for the deposit and dissemination of scientific research documents, whether they are published or not. The documents may come from teaching and research institutions in France or abroad, or from public or private research centers.

L'archive ouverte pluridisciplinaire **HAL**, est destinée au dépôt et à la diffusion de documents scientifiques de niveau recherche, publiés ou non, émanant des établissements d'enseignement et de recherche français ou étrangers, des laboratoires publics ou privés.

Long bone shape variation in the forelimb of Rhinocerotoidea – Relation with size, body mass and body proportions

Christophe Mallet[1], Alexandra Houssaye[1], Raphaël Cornette[2], Guillaume Billet[3]

1 Mécanismes adaptatifs et évolution (MECADEV), UMR 7179, MNHN, CNRS, 55 rue Buffon, CP 55, 75005, Paris, France

2 Institut de Systématique, Evolution, Biodiversité (ISYEB), UMR 7205, MNHN, CNRS, SU, EPHE, UA, 57 rue Cuvier, CP 50, 75005 Paris, France

3 Centre de Recherche en Paléontologie – Paris (CR2P), UMR CNRS 7207, MNHN, CNRS, SU, 8 rue Buffon, CP 38, 75005 Paris, France

Corresponding author:

Christophe Mallet

55 rue Buffon, CP 55, 75005, Paris, France

Email address: christophe.mallet@edu.mnhn.fr

Running title: **Bone shape variation in the forelimb of Rhinocerotoidea**

ABSTRACT

In quadrupeds, limb bones are strongly affected by functional constraints linked to weight support, but few studies have addressed the complementary effects of mass, size and body proportions on limb bone shape. During their history, Rhinocerotoidea have displayed a great diversity of body masses and limb bone relative size and proportions, from small tapir-like forms to giant species. Here, we explore the evolutionary variation of shape in forelimb bones and its relationship with body mass in Rhinocerotoidea. Our results indicate a general increase in robustness and greater development of muscular insertions in heavier species, counteracting the higher weight loadings induced by an increased body mass. The shape of the humerus changes allometrically and exhibits a strong phylogenetic signal. Shapes of the radius and ulna display a stronger link with body mass repartition than with the absolute mass itself. Congruent shape variation between the humerus and the proximal part of the ulna suggests that the elbow joint is comprised of two strongly covariant structures. In addition, our work confirms the uniqueness of giant Paraceratheriidae among Rhinocerotoidea, whose shape variation is related to both a high body mass and a cursorial forelimb construction.

KEYWORDS

Appendicular skeleton – Body mass – Brachypody – Functional morphology – Geometric morphometrics – Graviportality – Rhinoceros

INTRODUCTION

In tetrapods, limb bones play a dual role in supporting the body and ensuring an efficient locomotion in a given environment, while being intimately related to the muscles attached on them. The shape of the limb bones of quadrupeds is therefore highly related to body size, body mass and locomotor constraints (Hildebrand, 1974; Polly, 2007; Biewener & Patek, 2018). The strong tendency of many quadruped lineages to converge towards high body mass across their evolutionary history (Cope, 1887; Depéret, 1907; Raia *et al.*, 2012; Baker *et al.*, 2015; Bokma *et al.*, 2016) allows to highlight repeated patterns of musculoskeletal changes related to increase in size and weight for diverse morphologies. The condition of heavy animals is often called “graviportality” and classically opposed to “cursoriality”, which is encountered in running animals like horses and many other ungulate taxa (Hildebrand, 1974; Carrano, 1999). Many works investigated the skeletal features often found in “graviportal” tetrapods, such as more vertical and thicker limbs, a reorientation of girdle bones, changes in limb segment proportions, or an internal micro-anatomical restructuration (Gregory, 1912; Osborn, 1929; Hildebrand, 1974; Coombs, 1978; Eisenmann & Guérin, 1984; Biewener, 1989a,b; Bertram & Biewener, 1990; Houssaye, Fernandez, & Billet, 2016). These changes in body proportion are also linked with changes in locomotor capacities. All these modifications can lead to a high diversity of body plans for a single given mass (Hildebrand, 1974; Polly, 2007) and, consequently, to modifications of the bone shape. However, bone shape changes associated with body mass increase are poorly documented among quadrupeds.

Although only five species of modern rhinos survive today (Dinerstein, 2011), the Rhinocerotoidea was a flourishing superfamily during most of the Cenozoic. A rich and well-preserved fossil record led to the description of more than a hundred species distributed in Eurasia, North America and Africa, showing a huge diversity of ecological niches and locomotor conditions (Prothero & Schoch, 1989; Cerdeño, 1998; Prothero, 2005; Biasatti, Wang, & Deng, 2018). Rhinocerotoidea ranged from less than 100 kg in *Hyrachyus*, the most ancient representative of the superfamily (Antoine, 2002; Bai *et al.*, 2017), to between 10 and 17 tons in giant Paraceratheriidae (Fortelius & Kappelman, 1993; Prothero, 1998, 2013; Qiu & Wang, 2007; Larramendi, 2016) (Table 1). Between these two extremes, numerous lineages showed convergent increases in body mass, with many species exceeding 1 ton or more (Cerdeño, 1998). In addition to this variation in body mass, the evolutionary history of rhinocerotoids exhibit fluctuations in their general body plan (from cursorial to graviportal), their degree of brachypody (or gracility, i.e. reduction of their relative limb length), their ecological affinities (from open environments to presumed semi-aquatic lifestyles), their number of forelimb digits (tetradactyl or tridactyl manus), the presence, position and number of horns, and the size of their head, all of which may also have covaried with the shape of long bones (Guérin, 1989; Prothero

& Schoch, 1989; Prothero, 1998, 2005, 2013; Cerdeño, 1998; Antoine, 2002; Becker, 2003; Becker *et al.*, 2009; Bai *et al.*, 2017).

Consequently, members of the superfamily represent a rich diversity of body mass, size and proportions and constitute a great example for exploring how the evolution of long bone shape in the group could be associated with these parameters. A few studies previously investigated the shape variation of the limb bones in either modern or fossil rhinocerotoids, but rarely in regards to mass, size or degree of brachypody / gracility (Guérin, 1980; Prothero & Sereno, 1982; Becker, 2003; Mallet *et al.*, 2019, 2020; Etienne *et al.*, 2020). To date, no comprehensive morphofunctional analysis has explored covariation patterns between the shape of the long bones and each of these parameters at the scale of the entire superfamily.

Here, we investigate the shape variation of the forelimb bones among the superfamily Rhinocerotoidea in relation with bone size, body mass and degree of gracility. We performed phylogenetically-informed shape analyses of the three forelimb bones (humerus, radius, ulna) in a 3D geometric morphometric context. We chose to focus on forelimb bones because they play a crucial role in supporting the body weight and in braking during locomotion in quadrupeds (Hildebrand, 1974; Dutto *et al.*, 2006; Henderson, 2006). Previous works on modern rhinos indicate a greater association of both mass and size with the shape of the forelimb bones over that of the hind limb ones (Mallet *et al.*, 2019, 2020). In accordance with literature, we hypothesize: (a) a strong association of bone size, body mass, and degree of gracility with bone shape; (b) different expression of this association on the stylopodium and zeugopodium respectively (Alexander *et al.*, 1979; Prothero & Sereno, 1982; Biewener, 1989b; Bertram & Biewener, 1992; Mallet *et al.*, 2019, 2020); (c) a strong phylogenetic signal in bone shape variation, with differences depending on the considered bone. Testing these hypotheses will enable to precisely highlight whether and how body mass could have played a role in shaping the evolution of forelimb bones among rhinocerotoids.

MATERIAL AND METHODS

Studied sample

We selected 283 modern and fossil specimens housed in fifteen institutions and representing a total of 94 humeri, 105 radii and 84 ulnae (see Supplementary Table S1 for the complete list of studied specimens). The dataset included 69 taxa (5 modern and 64 fossil species) belonging to almost all families of the superfamily Rhinocerotoidea (no representative of the recently-defined family Eggysodontidae were included) (Fig. 1). Taxa were selected to include as much body shape and mass diversity as possible and to cover the largest temporal range but this selection also depended much on the available material. Taxonomic attributions were verified or updated using recent literature, directly with specimen numbers when available, or using taxonomic lists and institution databases for each locality. We retained the most recent binomial names considered as correct following the International Commission on Zoological Nomenclature rules (see Supplementary Table S1).

We only considered adult individuals with fully fused epiphyses. We chose complete bones displaying no or negligible taphonomic effects (e.g., shallow surface cracks not altering the global shape), rejecting specimens massively crushed or restored with plaster. We also considered uncomplete bones in partial shape analyses (see below), as long as they were not crushed or distorted. Almost no information regarding sex was available for fossil specimens: even if sexual dimorphism is known for some species and may slightly affect the shape of long bones (Guérin, 1980; Dinerstein, 1991; Mead, 2000; Zschokke & Baur, 2002; Mihlbachler, 2007; Chen *et al.*, 2010), we assumed that this intraspecific variation was largely exceeded by interspecific shape changes (according to Mallet *et al.*, 2019). For each species, we selected between up to three specimens for each bone. All anatomical terms follow classic veterinary terminology and anatomical works on Perissodactyla and rhinoceroses (Guérin, 1980; Federative Committee on Anatomical Terminology, 1998; Antoine, 2002; Prothero, 2005; Barone, 2010a; Heissig, 2012; Bai *et al.*, 2017). These terms are illustrated in Supplementary Figure S2. Locations of muscle insertions follows Etienne, Houssaye, & Hutchinson (2021).

3D models

Most bones were digitized with a structured-light three-dimensional scanner (Artec Eva) and reconstructed with Artec Studio Professional software (v12.1.1.12—Artec 3D, 2018). This software was also used to reconstruct bones broken in two or more pieces (without any lacking part) in a single complete mesh. Some specimens were digitized with a photogrammetric approach, following Mallison & Wings (2014) and Fau, Cornette, & Houssaye (2016). Sets of photos were used to reconstruct 3D models using Agisoft Photoscan software (v1.4.2—Agisoft, 2018). Two specimens were digitized using medical computed tomography scanners at the Royal Veterinary College, London

(Equine Hospital) and at the University of California, San Francisco (Department of Radiology & Biomedical Imaging). For these specimens, bone surfaces were extracted as meshes using Avizo software (v9.5.0—Thermo Fisher Scientific, 2018). As a few specimens displayed small lacking parts on the shaft, we used Geomagic Studio (v2014.3.0.1781—3D Systems Corporation, 2014) to fill holes. We used the "curvature filling" tool to ensure that the added polygons matched the curvature of the surrounding mesh. Finally, each mesh was decimated to reach 250,000 vertices and 500,000 faces using MeshLab software (v2016.12—Cignoni *et al.*, 2008). We performed our analyses on left bones: when left bones were not available in some specimens, we used mirrored right bones instead.

3D geometric morphometrics

The shape variation of our sample was analysed through a 3D geometric morphometrics approach, a widely-used methodology allowing to quantify and visualize the morphological differences between objects by comparing the spatial coordinates of points called landmarks (Adams, Rohlf, & Slice, 2004; Zelditch *et al.*, 2012). We quantified the bone shape placing a set of anatomical landmarks and curve and surface sliding semi-landmarks on the meshes, following Gunz & Mitteroecker (2013) and Botton-Divet *et al.* (2016). Anatomical landmarks and curves were placed on meshes using the IDAV Landmark software (v3.0—Wiley *et al.*, 2005). We created a template to place surface sliding semi-landmarks for each bone. The geometric location of landmarks and sliding semi-landmarks is derived from previous morphometric works on rhinoceros long bones (Mallet *et al.*, 2019, 2020) to cover the shape diversity of the sample (see Supplementary Data S3 for details on landmark numbers and locations). Two specimens (*Dicerorhinus sumatrensis* NHMUK ZE 1948.12.20.1 for the humerus and the ulna, and *Ceratotherium simum* RMCA 1985.32-M-0001 for the radius) were chosen to be the initial specimens on which all anatomical landmarks, curve and surface sliding semi-landmarks were placed. We selected these two individuals for their average shape and size ensuring that all points will be correctly projected on other bones despite the great shape and size ranges of the sample. These specimens were then used as templates for the projection of surface sliding semi-landmarks on the surface of all other specimens. Projection was followed by a relaxation step to ensure that projected points matched the actual surface of the meshes. Curve and surface sliding semi-landmarks were then slid to minimize the bending energy of a thin plate spline (TPS) between each specimen and the template at first, and then four times between the result of the previous step and the Procrustes consensus of the complete dataset. Therefore, all landmarks can be treated at the end as geometrically homologous (Gunz, Mitteroecker, & Bookstein, 2005; Gunz & Mitteroecker, 2013).

As we chose to work at the species level, we then computed and analysed species mean shapes (Botton-Divet *et al.*, 2017; Serio, Raia, & Meloro, 2020). After the sliding step, we computed a first

Generalized Procrustes Analysis (GPA) with all specimens to remove the effect of size, location and orientation of the different landmark conformations (Gower, 1975; Rohlf & Slice, 1990). Then we computed the Procrustes consensus (or mean shape) of each species in the same geometric space. These Procrustes consensuses were superimposed in a second GPA in order to pool all species means in a single morphospace. This process was repeated for each bone separately. As our dataset contained more variables than observations, we computed a Principal Component Analysis (PCA) to reduce dimensionality (Baylac & Frieß, 2005; Gunz & Mitteroecker, 2013) and visualize the distribution of the species in the morphospace. We also computed theoretical shapes associated with both minimum and maximum of the first two components of PCAs using a Thin-Plate Spline (TPS) deformation of a template mesh. Phylogenetic relationships between taxa (see below) were then plotted in the morphospace and compared to Neighbour Joining (NJ) trees computed on PC scores. Projection, relaxation, sliding processes, GPAs, PCAs and theoretical shape computation were conducted using the "Morpho" package (v2.8—(Schlager, 2017) in the R environment (v3.5.3—R Core Team, 2014). Phylogeny was plotted on the morphospace using the "geomorph" package (v3.2.1—Adams & Otárola-Castillo, 2013). NJ trees were computed with the "ape" package (v5.3—Paradis *et al.*, 2018a).

Analyses on partial bones

Fossil long bones of rhinoceros can show redundant breakage patterns due to various taphonomic agents throughout the diagenesis process, for example high sedimentary pressure on fragile anatomical areas, trampling by heavy animals after burial (Hullot & Antoine, 2020), scavenger action on parts containing marrow (Guérin, 1980). This is notably the case of the proximal part of the humerus or the olecranon process of the ulna, frequently damaged and preventing us to use some specimens in whole bone shape analyses. In order to include a higher number of relevant taxa in our sample despite these alterations, we performed analyses on partial bones presenting important lacking parts. We included complete bones as well in these analyses on partial bones. Following Bardua *et al.* (2019), we used curve sliding semi-landmarks to define artificial lines acting as a limit for the sliding of surface semi-landmarks and virtually remove damaged or lacking parts from analyses. These limit lines involved at least one anatomical landmark to ensure that they were geometrically homologous on all specimens. They were placed as well on complete bones, which were all included in analyses on partial bones. Limit lines were finally removed after the sliding process and before the GPA to consider only true biological shape information in our analyses. Three datasets were used: distal half of the humerus, ulna without olecranon tubercle and proximal half of the ulna (see Supplementary Information S3 for details on landmarks and sliding semi-landmarks in templates of partial bones).

Phylogenetic framework

Although recent publications refined the phylogenetic relationships within Rhinocerotoidea (Wang *et al.*, 2016; Tissier *et al.*, 2018) and within Ceratomorpha (Bai *et al.*, 2020), these studies only include a small part of all genera of rhinocerotoids known worldwide. To date, no comprehensive and consensual phylogeny of the whole superfamily Rhinocerotoidea exists. To assess the effect of phylogenetic relationships on shape variation, we constructed a composite cladogram using trees previously computed on cranio-dental and postcranial characters or molecular data. Branch relations, lengths and occurrence dates were reconstructed after the works of Cerdeño (1995), Antoine (2002), Antoine, Duranthon, & Welcomme (2003), Antoine *et al.* (2010, 2021), Prothero (2005), Boada-Saña (2008), Piras *et al.* (2010), Becker, Antoine, & Maridet (2013), Lu, 2013), Wang *et al.* (2016), Averianov *et al.* (2017), Tissier *et al.* (2018), Tissier, Antoine, & Becker (2020), Bai *et al.* (2020). We used the cladistic framework of Antoine *et al.* (2003) and Becker *et al.* (2013) to define families, subfamilies, tribes and subtribes (Fig. 1). The relationships between the five modern taxa remain controversial, especially regarding the position of the Sumatran rhinoceros (*Dicerorhinus sumatrensis*) and its extinct relatives (e.g. Tougard *et al.*, 2001; Orlando *et al.*, 2003; Fernando *et al.*, 2006; Price & Bininda-Emonds, 2009; Steiner & Ryder, 2011; Yuan *et al.*, 2014; Welker *et al.*, 2017; Cappellini *et al.*, 2019). It is likely that these uncertainties may be due to a hard polytomy at the base of the crown-group containing the five modern species (Willerslev *et al.*, 2009; Gaudry, 2017). We therefore chose to consider a hard polytomy in our analyses and to address phylogenetic uncertainties using an NNI procedure (see below).

To address the effect of phylogenetic relationships on shape data for each bone, we evaluated their phylogenetic signal by computing a multivariate K statistic (K_{mult}) on PC scores (Adams, 2014). This index allows the comparison between the rate of observed morphological change and that expected under a Brownian motion on a given phylogeny (Blomberg *et al.*, 2003; Adams, 2014). As the K_{mult} computation requires fully bifurcating trees, we removed polytomies using the function *multi2di* in the "ape" package (Paradis *et al.*, 2018). This function resolves polytomies by randomly creating a new branch with a null length from one branch of the polytomous node (Swenson, 2014; Paradis *et al.*, 2018). K_{mult} was then computed using the function *K.mult* in the "phylocurve" package (Goolsby, 2015).

Body mass, centroid size and gracility index

We explored the association of three variables related to body proportions and size (body mass, centroid size of the bone and gracility index) with the shape of each long bone of the forelimb within Rhinocerotoidea. Mean body mass (BM) of each species was retrieved from the literature, compiling

up to three estimations per species to compute mean BMs (see Table 1 and Supplementary Data S4). However, BM estimations are highly heterogenous and can vary by a factor of three for a single species depending on the considered method and morphological proxy (dental, cranial or postcranial measurements), the specimen developmental stage, and the geological formation. Moreover, regression equations for BM estimation were rarely developed for Perissodactyla or rhinoceroses only, resulting in potentially biased results for fossil Rhinocerotoidea (Prothero & Sereno, 1982). We managed to collect BM estimation for only 40 over the 69 taxa constituting our sample. Consequently, we chose to also consider the centroid size (CS) of each bone, which is classically used to address allometric variation, i.e. the shape variation linked to size (Zelditch *et al.*, 2012; Mitteroecker *et al.*, 2013; Klingenberg, 2016; Hallgrímsson *et al.*, 2019). Centroid size, defined as the square root of the sum of the square of the distance of each point to the centroid of the landmark set (Zelditch *et al.*, 2012), is known to be a good proxy of the mass of the animal (Ercoli & Prevosti, 2011; Cassini, Vizcaíno, & Bargo, 2012), especially for limb bones of rhinoceros (Mallet *et al.*, 2019; Etienne *et al.*, 2020). Given the large range of body shapes within Rhinocerotoidea (Fig. 1) and the fact that the same mass can be associated with both a slender or a robust body condition, we used the mean gracility index (GI-MC3) as an estimator of the degree of brachypody (see Table 1 and Supplementary Data S4). This index is computed dividing the transverse width of the third metacarpal by its maximal length and has been much used for rhinocerotoids (Colbert, 1938; Arambourg, 1959; Guérin, 1980; Cerdeño, 1998; Becker, 2003; Becker *et al.*, 2009; Scherler *et al.*, 2013). The higher the GI-MC3 value, the shorter the limb length: species with a high GI-MC3 value are considered as more brachypodial (or less gracile) than species with low values. We computed this index by measuring third metacarpals when available in collections or compiling up to three GI-MC3 values in the literature to compute mean GI-MC3. These metacarpals were mostly associated with long bones for modern species, and mostly associated with a similar locality for fossil species (Supplementary Data S4). We addressed the effect of phylogeny on log-transformed CS, log-transformed cubic root of the mean BM, and log-transformed mean GI-MC3 using the univariate K statistic (Blomberg *et al.*, 2003). We tested for correlation between these three variables respectively using a linear regression on Phylogenetic Independent Contrasts (Felsenstein, 1985). We used the function *contMap* of the "phytools" package (Revell, 2012) to plot these three variables along the phylogeny.

Variation patterns, and thus covariation, can be expressed and analysed at different levels: across species (evolutionary variation), within a species at a single developmental stage (static variation), within a species across developmental stages (ontogenetic variation) (Klingenberg, 2014). Here we explored the evolutionary covariation of bone shape with each of the three variables (BM, CS, GI-

MC3) considering a multivariate approach using Phylogenetic Generalized Least Squares (PGLS), a regression model taking into account the phylogenetic framework and computed here on Procrustes coordinates to quantify the shape variation related to CS, BM and GI-MC3 (Martins & Hansen, 1997; Rohlf, 2001; Klingenberg & Marugán-Lobón, 2013; Adams & Collyer, 2018). This was done using the function *procD.pgls* of the "geomorph" package (v3.2.1—Adams & Otárola-Castillo, 2013), suited for 3D geometric morphometric data. However, the function *procD.pgls* uses a Brownian Motion of evolution to compute PGLS, which assumes non-directional trait changes, while other models might assume a different computational hypothesis. To account for these changes depending on the considered model, we also computed PGLS under a Phylogenetic Ridge Regression model of evolution (Castiglione *et al.*, 2018). The Phylogenetic Ridge Regression allows to take into account variations of evolutionary rates along the different branches of a phylogenetic tree, accounting for potential accelerations and decelerations of the phenotypic changes among groups in a more accurate way than does a Brownian Motion. We therefore used the function *PGLS_fossil* of the 'RRphylo' package (v.2.5.0 – Castiglione *et al.*, 2018) to compute PGLS with a Ridge Regression model and compare it to the results obtained under a Brownian Motion model in order to see whether our results were robust to model variations.

As the phylogeny of Rhinocerotoidea remains debated for both extant and extinct taxa (see above), we assessed the effect of potential uncertainty in taxa position in the phylogeny on PGLS by using a Nearest Neighbour Interchange (NNI) procedure. NNI algorithm generates new trees by swapping two adjacent branches of a specified tree (Felsenstein, 2004). We generated new trees using the *nni* function of the package "phangorn" (Schliep, 2011) and computed PGLS with these rearranged trees to estimate the ranges of R^2 and p values.

All statistic tests have been considered as significant for p-values ≤ 0.01. However, given that recent statistical works call for a continuous approach of the p-value (Wasserstein, Schirm, & Lazar, 2019; Ho *et al.*, 2019), we chose to mention results having a p-value up to 0.05 as well.

RESULTS

Correlation between BM and GI-MC3

The evolutionary variations of mean BM and mean GI-MC3 both show a significant phylogenetic signal (K_{BM} = 1.75, p < 0.001; K_{GI-MC3} = 1.70, p < 0.001) and they are significantly correlated with one another when phylogeny is taken into account (r = 0.44, p < 0.001). The mapping of mean BM and GI-MC3 along the phylogeny (Fig. 2) clearly indicates that, despite this significant correlation, there is not a strict correspondence between high BM and high GI-MC3 values. This is particularly visible for Paraceratheriidae, large Elasmotheriinae and Teleoceratina.

Differences in PGLS between Brownian Motion and Phylogenetic Ridge Regression

PGLS computed under a Brownian Motion (BM) model (using the geomorph functions) and under a Phylogenetic Ridge Regression (RR) model (using the RRphylo functions) show similar results (see Supplementary Table S5 for detailed comparison between both models). Significant regressions under a BM model remain significant under a RR model, as well as non-significant results under a BM model remain non-significant under a RR model. R^2, p-values and shape deformations are extremely close in both cases. Only regression plots differ, those obtained under a RR model showing a much higher spread of specimens, making their interpretation more difficult. For all these reasons, we chose to present only results obtained under a BM model in the following sections.

Humerus – complete bone

The species distributions in the NJ tree (Fig. 3A) and in the phylomorphospace (Fig. 4A) computed on the complete humeri are mostly congruent with phylogeny, which is not surprising since the phylogenetic signal carried by its shape variation is strong (K_{mult} = 1.16, p < 0.01). Along the NJ tree, small-sized and early-diverging Hyrachyidae and Hyracodontidae are followed by a cluster mixing Rhinocerotidae and Rhinocerotinae *incertae sedis* (*i. s.*) with *Paramynodon* (Amynodontidae), *Urtinotherium* (Paraceratheriidae), *Menoceras* (Elasmotheriinae), some Aceratheriini and even *Dicerorhinus sumatrensis*. Other Aceratheriini are grouped close to Teleoceratina and *Dihoplus megarhinus* (Rhinocerotini), while almost all Rhinocerotina form a well-separated group (Fig. 3A). The phylomorphospace of the first two axes of the PCA, representing 63.7% of the global variance, is structured in a similar way (Fig. 4A). PC1 carries 54% of the variance. Along PC1, Hyrachyidae and Hyracodontidae plot towards negative values while *Paramynodon* is close to a central cluster grouping *Urtinotherium, Menoceras*, Aceratheriini, Teleoceratina, as well as Rhinocerotidae and Rhinocerotinae *i. s.* Within this cluster, *Aphelops* shares a shape proximity with all Teleoceratina, whereas other Aceratheriini are closer to more ancient taxa (*Amphicaenopus*, *Trigonias*,

Protaceratherium, *Plesiaceratherium*, and *Menoceras*). All members of the subtribe Rhinocerotina group together towards positive values, with *Stephanorhinus, Dicerorhinus, Dihoplus* and *Rhinoceros* overlapping the *Aphelops*-Teleoceratina cluster. The highest PC1 values are associated with the modern African clade (*Ceratotherium-Diceros*) and their extinct relatives, and the *Coelodonta* clade. PC2 represents 9.7% of the global variance. It is mainly driven by an opposition between Hyrachyidae, Hyracodontidae and Rhinocerotina towards negative values and Amynodontidae, Paraceratheriidae and all other Rhinocerotidae towards positive values. *Urtinotherium* is strongly isolated from all other species towards maximal positive values.

The shape variation along PC1 is mainly related to the bone slenderness (Fig. 3A and Supplementary Figure S6A). Towards the minimal values, the humerus is thin and straight, with a greater trochanter developed cranio-medially; an asymmetrical bicipital groove; a rounded humeral head oriented proximo-caudally; a poorly developed deltoid tuberosity; a poorly developed supracondylar crest; a narrow olecranon fossa; a symmetrical trochlea with a developed capitulum. The shape associated with maximal values is highly robust and thick, with a strong development of the lesser tubercle over the greater one; a large symmetrical bicipital groove with an intermediate tubercle; a deltoid tuberosity highly developed laterally; a strong development of the lateral epicondyle and the epicondylar crest; a large and rectangular olecranon fossa; an asymmetrical trochlea with a reduced capitulum. Along PC2, the shape variation mainly concerns epiphyseal elements. Towards positive maximum, the humerus displays a greater tubercle developed cranially; a rounded head oriented proximally; a strong deltoid tuberosity situated at the middle of the shaft; a larger shaft diameter; a strong proximo-lateral development of the epicondylar crest; a trochlea flattened proximo-distally. The shape associated with minimal values exhibits a deltoid tuberosity situated above the midshaft; a poorly developed epicondylar crest with a lateral epicondyle directed latero-distally; and an asymmetrical trochlea medially developed.

The evolutionary variation of the centroid size of complete humeri bears a significant phylogenetic signal (K_{CS} = 1.28, $p < 0.001$) and is highly correlated with BM ($r = 0.64$) and marginally correlated with GI-MC3 ($r = 0.37$, $p = 0.03$) (Table 2). PGLS results indicate that CS, BM and GI-MC3 are all significantly correlated with humerus shape (Table 3). NNI procedure indicates that the correlation with BM is more strongly affected by phylogenetic uncertainties than that with CS (Table 3). This may be related to a smaller and less diverse sample for BM values. Regression of shape against CS shows a very good fit to the regression line, most of the species following a marked common trend with little divergences far away from the line (Fig. 5A). Most of the Rhinocerotini (i.e., Rhinocerotina and Teleoceratina) are situated below the regression line while the other species are situated above. *Urtinotherium* appears as slightly shifted from the general trend. In the absence of many taxa such as

Hyracodontidae, Amynodontidae and Paraceratheriidae, regression of shape against BM shows a good fit to the regression line. The trend is strongly driven by *Hyrachyus*, which potentially constitutes a bias. However, a clear separation exists between Aceratheriini, all situated below the regression line, and Rhinocerotini, mainly situated above the line (Fig. 5B). Results for GI-MC3 indicate a very good fit to the regression line as well. Rhinocerotina group almost all together above the line while Teleoceratina are situated below the line. All other species are mixed close to the common trend. Hyrachyidae and Hyracodontidae are isolated towards minimal values (Fig. 5C). If shape variation related to these three variables mainly concerns an increase of robustness towards maximal values (Fig. 5 and Supplementary Data S7A, B, C), that related to BM (that lacks heavy Paraceratheriidae) is slightly different from those related to CS and GI-MC3, with a stronger medio-lateral development of both epiphyses relatively to the shaft (Fig. 5B). Most of the shape variation occurs on the medial face of the bone and on strong muscular insertions like the deltoid tuberosity and the epicondylar crest for the three variables. In addition, BM variation affects the bicipital groove while variation of GI-MC3 implies shape changes located distally and caudally to the humeral head, from the deltoid tuberosity and tricipital line to the lesser tubercle convexity (Fig. 5C).

Humerus – distal part

The phylogenetic signal carried by the shape variation of the distal humeri is strong (K_{mult} = 1.22, $p < 0.01$). The species distributions in the NJ tree (Fig. 3B) and in the phylomorphospace are highly similar to those observed for the complete humeri (Fig. 4B). On the NJ tree, all Amynodontidae are grouped together with *Juxia* (small Paraceratheriidae) while giant Paraceratheriidae group together close to some Aceratheriini (*Aphelops*, *Chilotherium*). Other Aceratheriini are mixed with Teleoceratina and more basal taxa, while Rhinocerotina form a homogeneous cluster all together. A similar organisation is observable in the phylomorphospace, where the first two axes represent 70.2% of the global variance. PC1 carries 55% of the global variance and PC2 carries 15.2%. The species distribution along both axes is largely similar to that observed for the complete humerus (Fig. 4B). Small and large Amynodontidae group together with the light paraceratheriid *Juxia*, while heavier Paraceratheriidae form an isolated cluster along PC2. Within Rhinocerotina, species seem distributed from the smallest to the largest along PC1 despite some exceptions (e.g., *Dihoplus megarhinus*, *Rhinoceros unicornis*). *Chilotherium* shows the highest positive value on PC1.

The shape variation along PC1 is highly similar to that observed on complete bones (Fig. 4B and Supplementary Figure S6B). Towards positive maximal values, PC1 is mainly associated with an increase of thickness, with a strong development of the epicondylar crest; a broad olecranon fossa;

385 an asymmetrical trochlea with a reduced capitulum. Along PC2, the shape variation is also almost
386 identical to that observed on complete bones.

387 The evolutionary variation of the centroid size of partial humeri carries a significant phylogenetic
388 signal (K_{CS} = 1.39, $p < 0.001$). The correlation between CS and BM is higher than for the complete
389 humeri (r = 0.72) and correlation between CS and GI-MC3 is significant (r = 0.50) (Table 2). Like for
390 complete bones, PGLS results indicate a significant correlation between humerus shape and CS, BM
391 and GI-MC3, respectively. NNI procedure indicates that phylogenetic uncertainties do not highly
392 affect the relation between shape and the three variables (Table 3). The regression plot of shape
393 against CS indicates an excellent fit to the regression line with a tendency similar to that observed on
394 complete bones, but with Hyrachyidae, Hyracodontidae, Amynodontidae and Paraceratheriidae
395 slightly shifted towards less robust shapes for a given CS than Rhinocerotidae, which have a
396 generalized "large-and-heavy-head" plan, with respect to other families among Rhinocerotoidea.
397 (Fig. 6A). The presence of Amynodontidae and Paraceratheriidae in the regression of shape against
398 BM highlights a strongly similar tendency and a very strong fit to the regression line (Fig. 6B). The
399 regression plot of shape against GI-MC3 is almost identical to that obtained on complete bones with
400 a good fit to the regression line as well (Fig. 6C). Similarly, the shape variation is very similar to that
401 of complete bones for the three variables, mainly affecting the general robustness and muscular
402 insertions such as the epicondylar crest that is broadened (Fig. 6 and Supplementary Data S7D, E, F).
403 Only the shape variation associated with BM slightly differs with an epicondylar crest less developed
404 than for complete bones towards maximum values.

405 **Radius**

406 Like for the humerus, the phylogenetic signal carried by shape data of the radii is strong (K_{mult} = 1.15,
407 $p < 0.01$). However, the species distributions in the NJ tree (Fig. 3C) and in the phylomorphospace
408 (Fig. 7) are less reminiscent of the phylogeny and seem likely related to the degree of brachypody.
409 Along the NJ tree, Hyrachyidae group with Hyracodontidae, Paraceratheriidae and small
410 Elasmotheriinae. Aceratheriini, Teleoceratina and Rhinocerotina are mixed together with larger
411 Elasmotheriinae, most of the species being sorted by their gracility rather than mass or size. This
412 pattern is highly similar to that seen on the PCA, with the first two axes representing 75% of the
413 global variance (Fig. 7). PC1 gathers 70.7% of the global variance. Along this axis, *Triplopus*
414 (Hyracodontidae) constitutes the positive maximum. Contrary to the morphospace obtained for the
415 humerus, two of the biggest species of the sample, *Juxia* and *Urtinotherium* (Paraceratheriidae), plot
416 together with the smallest and lightest species. *Paraceratherium* groups with small Elasmotheriinae
417 and Rhinocerotidae *i. s.*, as well as *Amynodon* and *Paramynodon* (Amynodontidae). Towards negative

values, Aceratheriini, Rhinocerotini (Teleoceratina and Rhinocerotina) are grouped together with larger Elasmotheriinae (*Hispanotherium* and *Elasmotherium*). Within this cluster, *Stephanorhinus, Dicerorhinus* and some *Dihoplus* plot with *Aphelops, Peraceras* and *Hoploaceratherium*, whereas larger Rhinocerotina (*Ceratotherium, Rhinoceros, Diceros, Coelodonta*) are closer to *Brachypotherium* and *Diaceratherium* (Teleoceratina). Only *Teleoceras* and *Coelodonta antiquitatis* plot outside the main cluster towards the maximal negative values. PC2 represents only 4.3% of the variance and no obvious organisation of the specimens is visible along this axis.

Like for the humerus, the shape variation of the radius along PC1 is mainly related to the bone slenderness (Fig. 7 and Supplementary Figure S6C). The shape associated with maximal values is thin and slender, with slight cranio-caudal and medio-lateral bends; a rectangular glenoid cavity with a lateral expansion for the capitulum; a shaft as large medio-laterally as the two epiphyses; a rectangular and shallow distal articular surface; a poorly developed radial styloid process. Conversely, the shape associated with the minimal values is massive with a large asymmetrical glenoid cavity; almost no lateral development of the cavity for the capitulum; both epiphyses medio-laterally larger than the diaphysis; a radial styloid process developed distally; a rectangular and deep distal articular surface.

Like for humerus, the evolutionary variation of the centroid size of the radius carries a significant phylogenetic signal ($K_{CS} = 0.82$, $p < 0.001$). The correlation between CS and BM is significant and high ($r = 0.80$) whereas CS and GI-MC3 are not correlated (Table 2). PGLS results indicate that the radius shape is significantly correlated with BM and GI-MC3 respectively, the latter correlation being stronger than the former (Table 3). PGLS computed on NNI trees indicate that correlation with BM is affected by phylogenetic uncertainties and may be non-significant depending on the tree configuration. Conversely, correlation with CS appears as always non-significant and GI-MC3 as always significant for whatever the tree configuration (Table 3). The regression plot of radius shape against BM indicates a rather good fit to the regression line (Fig. 8A). Paraceratheriidae and *Teleoceras* deviate strongly from the common regression trend, while Rhinocerotina and Elasmotheriinae strongly follow it. The shape variation associated with maximal values of BM is mainly related to a medio-lateral development of both epiphyses, notably on the lateral part of the proximal epiphysis, where inserts the *m. biceps brachii* (Etienne *et al.*, 2021). These changes are also associated to a slight increase of robustness towards high BM values (Fig. 8A and Supplementary Figure S7G). The regression plot of shape against GI-MC3 indicates an excellent fit to the regression line, with a strong common trend shared by all members of the superfamily. Although most Rhinocerotina are situated above the regression line, they are mixed together with Aceratheriini, Teleoceratina and large Elasmotheriinae. Giant Paraceratheriidae plot together with small

Elasmotheriinae and almost all Amynodontidae, while the small paraceratheriid *Juxia* is close to *Hyrachyus* and *Hyracodon*. *Triplopus* plots towards minimal values (Fig. 8B). GI-MC3 variation is correlated with a medio-lateral development of the bone appearing stronger on the lateral side of both epiphyses than on the medial one, although less marked than for BM (Fig. 8B and Supplementary Figure S7H), and with an overall increase in robustness.

Ulna – complete bone

The shape variation of the complete ulnae carries a strong phylogenetic signal (K_{mult} = 0.93, $p < 0.01$). The NJ tree (Fig. 3D) shows a grouping of Hyrachyidae, Hyracodontidae, small Elasmotheriinae and *Juxia* (which slightly isolates from this cluster). Aceratheriini group together with some *Diaceratherium* but also the Amynodontidae, while all other Teleoceratina are grouped together and slightly isolate from other species. *Metamynodon* (Amynodontidae) is placed between Aceratheriini and Teleoceratina, while all Rhinocerotina group together (also with *Dia. lamilloquense*). A similar structure is observed on the phylomorphospace, with the first two axes representing 70.2% of the global variance (Fig. 9A). The first axis carries 54.7% of the variance. *Juxia* (Paraceratheriidae) plots towards minimal values. Small Elasmotheriinae group together with *Trigonias*, *Protaceratherium* (Rhinocerotidae *i. s.*) and *Paramynodon* (Amynodontidae) towards minimal values. However, *Amphicaenopus* and *Metamynodon* group with a cluster containing Aceratheriini and Rhinocerotini, as well as some *Diaceratherium*. Within Rhinocerotina, larger taxa such as *Ce. simum*, *R. unicornis*, *Co. antiquitatis* or *Dh. pikermiensis* group towards slightly higher values. *Prosantorhinus*, *Brachypotherium, Dia. aurelianense* and *Teleoceras* constitute the highest positive values. The second axis accounts for 15.5% of the global variance. *Hyrachyus* and Rhinocerotina group together in the negative part of the axis with almost no overlapping of the other species. Rhinocerotidae *i. s.* plot around null values together with *Hyracodon*, Amynodontidae, small Elasmotheriinae, *Hoploaceratherium* and *Dia. lamilloquense*. All other Teleoceratina group with Aceratheriini and *Juxia* towards the highest positive values.

Like for the humerus and the radius, the shape variation of the ulna along PC1 is mainly related to the bone slenderness (Fig. 9A and Supplementary Figure S6D). The shape associated with minimal values is highly thin and slender with an olecranon tuberosity developed proximally; a symmetrical and medio-laterally flattened articular surface for the humerus; a shaft bended in cranio-caudal direction and highly compressed medio-laterally; a narrow and shallow distal articular surface; an articular surface for the pisiform developed proximally. Conversely, the shape associated with maximal values is robust and massive with a strong olecranon tuberosity developed proximo-caudally; a large and asymmetrical articular surface for the humerus; a massive and straight shaft

with a triangular section; a distal epiphysis developed medio-laterally; a distal articular surface wide and deep; a reduced articular surface for the pisiform. Along PC2, the shape associated with minimal values display an olecranon tuberosity developed proximo-distally; an anconeus process developed cranially; a shaft bended cranio-caudally; a narrow distal articular surface. The shape associated with maximal values displays an olecranon tuberosity developed mainly caudally; an anconeus process poorly developed cranially; a shaft with a curved caudal border and a straight cranial border; a wide and medially tilted distal articular surface.

The evolutionary variation of the centroid size of the complete ulnae carries a significant phylogenetic signal (K_{CS} = 0.84, p = 0.002). Centroid size is not significantly correlated with GI-MC3 and marginally significantly correlated with BM (r = 0.44, p = 0.04) (Table 2). PGLS results highlight only a strong and significant correlation between the ulna shape and GI-MC3 (Table 3). PGLS computed on NNI trees confirm that neither BM nor CS are significantly correlated with shape whatever the phylogenetic configuration (Table 3). Like for the radius, the regression plot of shape against GI-MC3 shows a very good fit to the regression line and highlights a strong common trend with few outliers. However, groups are more clearly separated than for the radius, with almost all Rhinocerotina plotting above the regression line, while other species plot below the line. Teleoceratina and Aceratheriini form well-separated groups with few overlapping with other species. Small Elasmotheriinae plot with Amynodontidae while *Hyrachyus* (Hyrachyidae) and *Juxia* (Paraceratheriidae) plot towards minimal values (Fig. 10A). A higher GI-MC3 is associated with a more robust and straighter ulna, showing a cranio-caudal and medio-lateral broadening and a strong development of the olecranon tubercle, as well as a development of the lateral insertion area for digit extensors along the shaft (Fig. 10A and Supplementary Figure S7I).

Ulna – without the olecranon tuberosity

Shape data of the ulna without the olecranon tuberosity carry a strong phylogenetic signal (K_{mult} = 0.81, p < 0.01). The NJ tree (Fig. 3E) and phylomorphospace (Fig. 9B) are very similar to those obtained for the complete ulnae. One of the main differences with the complete ulna is the position of the heavy *Elasmotherium* (Elasmotheriinae): the NJ tree highlights that this genus shares shape similarity with poorly related taxa like *Amphicaenopus* (Rhinocerotidae *i. s.*) and *Metamynodon* (Amynodontidae). On the phylomorphospace, the two first axes of the PCA account for 68.9% of the global variance. PC1 represent 51.5% while PC2 accounts for 17.4%. Again, *Elasmotherium* plots far away from smaller Elasmotheriinae like *Subhyracodon* and *Menoceras* along PC1, and closer to *Amphicaenopus*, *Metamynodon and Aphelops* (Fig. 9B). The shape variation associated with both axes is largely equivalent to that observed for the complete ulna (Fig. 9B and Supplementary Figure

S6E). PC1 is mainly driven by a change of slenderness and proportion of both epiphyses relatively to the shaft, with a highly massive and robust bone towards positive maximum. PC2 is mainly driven by changes of both orientation of the olecranon development and straightness of the shaft. Towards minimal values, the olecranon is oriented almost completely caudally and the cranial border of the shaft is fully straight.

Like for the complete ulna, the evolutionary variation of the CS of the ulna without olecranon carries a significant phylogenetic signal (K_{CS} = 0.78, p = 0.003). Conversely, CS is significantly and strongly correlated with BM (r = 0.52) but not with GI-MC3 (Table 2). Results of the PGLS indicate only a significant correlation between shape and GI-MC3, which is not affected by phylogenetic uncertainties. Conversely, the correlation between shape and CS remains non-significant regardless of phylogenetic uncertainties (Table 3). If the regression plot displays a trend relatively similar to that observed on complete ulnae, the fit to the regression line is poorer. Rhinocerotini (Rhinocerotina and Teleoceratina) are much more distant from the common regression slope, contrary to what it is observed for the radius and complete ulna. *Elasmotherium* and *Amphicaenopus* plot close to Rhinocerotina, which form a well-isolated cluster above the regression line (Fig. 10B). Shape variation related to GI-MC3 is highly similar to that observed along PC1, with a much more pronounced variation along the lateral side of the shaft (Fig. 10B and Supplementary Figure S7J). As observed on the radius, PGLS computed on BM display marginally non-significant results and NNI trees lead to significant or non-significant correlations between shape and BM depending on the considered phylogeny (Table 3). The regression plot shows a rather good fit to the regression line, despite some clear outliers. Most Rhinocerotina plot below the regression line, together with some Teleoceratina, while Aceratheriini form a central cluster. *Elasmotherium* plots towards maximal values while *Menoceras* plots towards negative values. This poorly significant regression can be related to the isolation of *Juxia* away from the common trend (see Supplementary Figure S8 for regression plot). The shape variation related to BM mainly concerns the caudal border of the ulna, particularly the area placed distally to the olecranon (see Supplementary Figure S8).

Ulna – proximal part

Shape data of the proximal parts of the ulnae carry a strong phylogenetic signal (K_{mult} = 0.72, p < 0.01). The NJ tree (Fig. 3F) and the phylomorphospace (Fig. 9C) show marked differences with previous analyses on the complete bones or on the ulna without the olecranon tubercle. The NJ tree is more congruent with phylogenetic groupings than is the phylomorphospace (Fig. 3F and 9C). Rhinocerotina form a homogeneous cluster (except for *Lartetotherium*) close to a group containing small Elasmotheriinae, *Protaceratherium*, *Hyracodon* and *Hyrachyus*. Aceratheriini and Teleoceratina

551 are mixed together. Paraceratheriidae and Amynodontidae plot with *Amphicaenopus*
552 (Rhinocerotidae *i. s.*) among the Aceratheriini-Teleoceratina group. On the phylomorphospace, the
553 two first axes of the PCA carry 55.2% of the global variance (Fig. 9C). PC1 represent 31.1% of the
554 global variance. Along this axis, *Hyrachyus* is isolated towards positive values. *Hyracodon*
555 (Hyracodontidae) and Amynodontidae plot in a cluster grouping Rhinocerotina, Elasmotheriinae and
556 Rhinocerotidae *i. s.* Aceratheriini and Teleoceratina isolate towards negative values.
557 Paraceratheriidae are placed between the Rhinocerotina cluster and the Aceratheriini-Teleoceratina
558 one, together with other taxa like *Lartetotherium, Metamynodon* and *Amphicaenopus*. The second
559 axis, representing 24.1% of the variance, is mainly driven by the isolation of Paraceratheriidae from
560 all other species, especially the two big forms of the genus *Paraceratherium*, towards minimal values.
561 Almost all other species form a single and mixed cluster from null to positive values without any clear
562 organisation.

563 Like for the complete ulna, the shape variation of the proximal part of the ulna along PC1 mainly
564 relates to the slenderness of the bone (Fig. 9C and Supplementary Figure S6F). The shape associated
565 with maximal values is thin and slender with a high olecranon tuberosity, developed in proximal
566 direction and medio-laterally flattened; an anconeus process developed cranially; a symmetrical
567 articular surface for the humerus flattened medio-laterally; a long synostosis surface for the radius.
568 Conversely, the shape associated with minimal values is thick and massive, with a strong olecranon
569 tubercle developed proximo-caudally and enlarged medio-laterally; an anconeus process poorly
570 developed; a wide and asymmetrical articular surface for the humerus; a short synostosis surface for
571 the radius. Along PC2, the variation is mainly driven by the proportion, shape and orientation of the
572 olecranon. Towards minimal values, the proximal part of the ulna displays a massive and short
573 olecranon, medio-laterally compressed and poorly caudally developed; a large and trapezoid articular
574 surface for the humerus; a poorly-developed anconeus process; a long synostosis surface for the
575 radius developed medially. The shape associated with maximal values displays a thinner and squared
576 olecranon developed proximo-caudally; a more triangular articular surface for the humerus; a short
577 synostosis surface for the radius.

578 The evolutionary variation of the centroid size of the proximal part of the ulna carries a significant
579 phylogenetic signal (K_{CS} = 1.91, $p < 0.001$). Like for the ulna without the olecranon tuberosity, the
580 centroid size is significantly and very strongly correlated with BM (r = 0.85) but not with GI-MC3
581 (Table 2). PGLS indicate a significant correlation between shape and each of the three variables,
582 similarly to what is observed on the complete and partial humerus (Table 3). However, both
583 regression plots of shape against CS and BM must be considered with caution, as the dispersion of
584 specimens poorly fits the regression line. For CS, Aceratheriini and Teleoceratina form a cluster

situated below the regression line, together with *Protaceratherium* and small Elasmotheriinae, while Rhinocerotina plot near the line. Paraceratheriidae, Amynodontidae and Rhinocerotidae *i. s.* plot above the line, while *Hyrachyus* plots towards minimal CS values (Fig. 11A). Similarly, for BM, Hyrachyidae and Paraceratheriidae plot far away from the common regression slope, whereas among Rhinocerotidae, some Aceratheriini and Teleoceratina are grouped together below the line (Fig. 11B). Conversely, the regression plot for the GI-MC3 is very close to those obtained on the humerus and radius, with an excellent fit to the regression line. All species are very close to the common regression line, with a marked overlap between the different groups (Fig. 11C). Shape variation related to both CS, BM and GI-MC3 is highly similar and mainly concerns a medio-lateral broadening towards high values, as well as a caudal development of the caudal border of the ulna (Fig. 11 and Supplementary Figure S7K, L, M). This broadening is more marked for shape variation correlated with GI-MC3.

Evolution of CS values along the phylogeny

The evolution of CS values along the phylogeny for the distal part of the humerus, complete radius and proximal part of the ulna (these three samples being the largest) is relatively congruent between the different taxa (Fig. 12). Hyrachyidae-Hyracodontidae and giant Paraceratheriidae possess, respectively, the lowest and highest values for each bone. However, the CS of the radius shows a greater variation along the phylogeny than that of the humerus and ulna. Many taxa among Elasmotheriinae, Aceratheriini and Teleoceratina display low values relatively to those observed on the humerus and ulna, these two bones displaying similar patterns of CS variation.

DISCUSSION

Relations between bone shape and mass, size and gracility

Our results highlight the strong relations existing between the shape variation of the forelimb bones and the changes in bone size, body mass and degree of gracility within Rhinocerotoidea, confirming the first hypothesis. However, these relations appear complex and variable depending on the bone, the anatomical area and the considerer parameter, resulting in congruent and non-congruent changes along the limb.

Congruent shape variation associated with all variables

Centroid size appears almost always significantly correlated with body mass, despite missing data, heterogeneous weight estimations and marginally non-significant results for the complete ulna. This suggests that the CS of the long bones is relevant to approximate the weight of a species (Ercoli & Prevosti, 2011; Cassini *et al.*, 2012; Botton-Divet *et al.*, 2017), at least on rhinocerotoids despite their diversity of body size and shape. However, beyond this general strong correlation, the variation of CS along the phylogeny for the radius differs from that observed for the humerus and ulna. Some groups may also strongly differ from the general trend shown by the whole superfamily because of specific morphological changes (i.e., Teleoceratina) (see below). Conversely, while BM correlates with GI-MC3, the latter is poorly related to CS except for the distal part of the humerus (and marginally for the complete humerus and proximal part of the ulna). This highlights that, beyond the significant correlation between bone size and body mass, these parameters do not vary conjointly with the degree of brachypody among the superfamily.

The complete humerus, distal humerus and proximal ulna share strong similarities in having their shape variation always correlated with CS, BM and GI-MC3. An increase of these variables is always associated with an increase of the bone robustness, confirming previous observations on modern (Mallet *et al.*, 2019, 2020) and fossil rhinocerotoids (Prothero & Sereno, 1982; Etienne *et al.*, 2020). Other areas mainly impacted by shape modification across the superfamily are epiphyses, which mainly extend in the medio-lateral direction in heavy species. These global changes tend to indicate the existence of a common trend within the entire superfamily Rhinocerotoidea for these bones, where shape varies relatively congruously with size, mass and gracility despite the morphological diversity of these species. Convergent shape tendencies may be observed among tetradactyl and tridactyl species respectively (see Supplementary Figure S9 for visualisation of shape variation depending on the digit number) but as the number of digits strongly follows the phylogeny, our results do not allow us to go any further on this issue.

637 The shape changes linked to size, mass or gracility are particularly congruent on the humerus,
638 affecting mainly the medial side of the bone, from the lesser tubercle tuberosity where inserts the *m.*
639 *subscapularis* to the midshaft where insert the *m. teres major* and the *m. latissimus dorsi*, these
640 muscles acting as adductors and extensors of the arm (Etienne *et al.*, 2021). On the lateral side, most
641 shape changes are located on the deltoid tuberosity, where inserts the *m. deltoideus* (Etienne *et al.*,
642 2021), being more laterally developed and more distally situated on the shaft for high values of body
643 mass, centroid size and gracility index (with a maximum for GI-MC3 – see below). This distal
644 displacement of the *mm. deltoideus* and of the *teres major* is coherent with an increase in strength of
645 the lever arm for arm flexion and extension required to move heavier body and limbs (Hildebrand,
646 1974; Polly, 2007). Such a distal displacement observed simultaneously among taxa opposed in
647 gracility and body mass (like Teleoceratina and Paraceratheriidae) can appear paradoxical. A longer
648 and stronger lever arm in large Paraceratheriidae is likely related to longer and heavier limbs
649 requiring more strength to be moved. Similarly, this condition in highly brachypodial taxa may result
650 from a difference in mass repartition: a lower centre of gravity associated with a relatively high body
651 mass and small limbs require powerful muscles with strong insertions to move efficiently
652 (Hildebrand, 1974; Coughlin & Fish, 2009; Biewener & Patek, 2018). Similar observations can be done
653 for the distal epiphysis, where most of the changes are located on the medial and lateral epicondyles
654 and the epicondylar crest when mass, size and brachypody increase. These changes are likely
655 associated with the development of powerful muscles for the extension movements of carpals and
656 digits (Fisher, Scott, & Naples, 2007; Barone, 2010a; Etienne *et al.*, 2021) and can relate to changes in
657 mass repartition and position of the centre of gravity as well.

658 Contrary to what is observed for the humerus and the proximal ulna, the shape variation of the
659 radius and ulna (complete and without the olecranon) are only significantly correlated with body
660 mass and gracility index (although marginally for the former parameter for the ulna). Both the radius
661 and ulna show a reduction of the cranio-caudal curvature and a straightening of the shaft with
662 increasing body mass and brachypody. These changes are coherent with modifications observed on
663 the humerus, highlighting the necessity to resist both higher pressure forces and stronger bending in
664 brachypodial species (Bertram & Biewener, 1992; Milne, 2016; Henderson *et al.*, 2017). On the ulna,
665 the congruent changes observed along the caudal edge of the bone towards high body mass and
666 degree of brachypody are likely linked to a modification of the orientation of the olecranon
667 tuberosity (see below).

668 *Non-congruent shape variation associated with variables*

Beyond congruent shape variations between bones or body proportions (size, mass and gracility), some anatomical areas appear to vary more in association with one particular variable. On the humerus, this is likely the case of the bicipital groove, which is reoriented cranially and becomes more symmetrical with the apparition of an intermediate tubercle for high body mass only. This conformation is likely to play a role as a "passive stay-apparatus", a feature convergently present in modern and some fossil horses as well, reducing the muscular energy needed to stand for long periods (Hermanson & MacFadden, 1992). A relatively developed intermediate tubercle is observed in many groups showing high body mass (Paraceratheriidae, Aceratheriini, Rhinocerotina, Teleoceratina and, to a lesser extent, Amynodontidae), indicating the presence of a partially or fully functional passive stay-apparatus in these heavy species. Although this feature in horses is associated with a cursorial condition, equids spending long periods of time in a standing pose, its development among Rhinocerotoidea appears mainly related to their body mass.

A pronounced development of the radial tuberosity, where inserts the *m. biceps brachii* (Etienne *et al.*, 2021), is observable on the radius. This development is only associated with body mass increase. This may be related to the strong flexion forces exerted by this muscle on the radius, likely related to the strength needed to move heavier limbs in large taxa (or a relatively short limb in species with a low centre of gravity). Moreover, the *m. biceps brachii* is also a relevant muscle involved in the passive-stay apparatus of the shoulder joint (Hermanson & MacFadden, 1992). The development of the radial tuberosity in association with body mass only is therefore coherent with changes observed on the humeral bicipital groove for the same variable.

On the ulna, the lateral border of the shaft shows a marked variation associated only with a high degree of brachypody. This area corresponds to the insertion of the lateral digit extensors (Etienne *et al.*, 2021) and its development is coherent with that observed on the epicondylar crest of the humerus (see above). Like for other extensors previously described, the marked development of these insertions along the ulna in brachypodial species may relate to the lowering of the centre of gravity and the higher power needed to move efficiently a short-limb body.

Congruent variations between bones

Congruent shape variations are also observed between bones, which partially infirm the second hypothesis. The tricipital line running from the deltoid process to the humeral head on the humerus is particularly affected by changes in the degree of brachypody. This area corresponds to the insertion of the lateral head of the *m. triceps brachii* (Etienne *et al.*, 2021). On the proximal ulna, an increase of size and mass, but above all of brachypody, involves morphological changes of the olecranon tuberosity, where inserts the tendon of the *m. triceps brachii* as well (Etienne *et al.*, 2021),

one of the most powerful extensors of the forelimb ensuring stance of the body and opposing to gravity (Watson & Wilson, 2007; Barone, 2010b; Etienne *et al.*, 2021). Furthermore, the development of its insertion is associated with a reorientation of the whole olecranon towards high body mass and degree of brachypody. These changes indicate a wider angle for elbow opening and a modification of the angulation of the olecranon process relatively to the shaft, known to strongly change with body mass among quadrupeds (Jenkins, 1973; Fujiwara, 2009; Fujiwara & Hutchinson, 2012; Milne, 2016; Henderson *et al.*, 2017).

Similarly, the distal trochlea of the humerus undergoes strong changes linked simultaneously to increases in mass, size and brachypody, becoming asymmetrical, wider and flattened, with a drastic reduction of the capitulum and a huge development of the medial lip. This conformation responds to changes observed on the radius and ulna when mass and brachypody increase. The proximal articular surfaces of the radius and ulna, forming the trochlear notch, lose their asymmetry and concavity in brachypodial taxa. Such coherent changes of the elbow region confer more degrees of freedom in the medio-lateral direction, contrary to the structure encountered in light and cursorial rhinos only allowing cranio-caudally constrained movements. This likely allows the elbow joint to support stronger constraints in multiple directions due to heavy weight (Polly, 2007). Such changes are coherent with similar modifications observed on the ankle joint of Rhinocerotoidea (Etienne *et al.*, 2020), but also with observations made on modern rhinocerotoids (Mallet *et al.*, 2019), indicating a development of the medial parts of limb bones over lateral ones for heavier species. All these morphological modifications in the elbow region, directly linked to a higher mass in heavy taxa, may relate to a lowering of the centre of gravity of the animal in brachypodial species, involving more muscle power and longer lever arms when associated with shorter limb segments for a given mass (Hildebrand, 1974).

Differences between the stylopodium and zeugopodium

Beyond these coherent changes located on precise anatomical areas, the patterns of shape variations appear very different between the stylopodial and the zeugopodial elements. While the variations of the humeral shape follow a trend common to the whole superfamily and are simultaneously related to size, mass and gracility, those of the radius and the ulna are highly related to the degree of brachypody, coupled with an effect of the body mass being more marked on the radius than on the ulna. This relation between shape and brachypody is strikingly high for the radius. All these results likely indicate a deep functional breakdown between the stylopodium and the zeugopodium. This is coherent with an increase of the variation of limb elements along a proximo-distal gradient, as hypothesized by previous authors (Hallgrímsson, Willmore, & Hall, 2002; Young & Hallgrímsson,

2005). Thanks to its obliquus orientation in the limb, the humerus ensures weight support by allowing the dissipation of stresses, while also being the support of muscles linked both to the pectoral girdle and the carpals. It therefore ensures the flexion and extension of the whole forelimb (Polly, 2007). At the opposite, the radius and the shaft of the ulna, oriented vertically, are strongly aligned with pressure constraints due to gravity. The proximal articular surface of the radius supports the entirety of the humerus and, consequently, a significant part of the body weight – the forelimb itself supporting a larger proportion of the total weight than the hind limb (Henderson, 2006; Regnault *et al.*, 2013; Stilson, Hopkins, & Davis, 2016; Panagiotopoulou, Pataky, & Hutchinson, 2019). Results highlight however that the zeugopodial shape is more highly related to variations of brachypody than of weight, underlining the importance of the repartition of mass in the body and the position of the centre of gravity, rather than to the absolute body mass itself. The influence of the body mass value itself is more visible at lower taxonomic levels (i.e. within families or subfamilies), as it has been observed among modern rhinos (Mallet *et al.*, 2019, 2020).

Modularity of the elbow joint

Beyond the congruences previously described between the humerus and the ulna, the exploration of the shape of both complete and partial bones, driven at first by taphonomic constraints, led to unexpected functional observations. Whereas the complete and distal humerus show similar results, strong differences occur between the whole ulna and its proximal part (in their relations between shape, size, mass and gracility, while the shaft and the distal part seem to follow the same pattern as the radius. The proximal part of the ulna displays similar patterns of variation as the humerus ones (complete and distal), its shape being not only linked to gracility as in the complete ulna, but also to mass and size. This is particularly visible in Paraceratheriidae, whose complete ulna is close to the plesiomorphic condition but whose proximal part of the ulna shows a derived morphology coherent with that of the humerus. Additional analyses on the isolated proximal part of the radius do not show this morphological shift and led to results highly similar to those obtained on complete radius (C. M., pers. obs.). The elbow is known as a simple yet crucial hinge joint among quadrupeds, involved both in locomotion and stability of the body (Jenkins, 1973; Fujiwara, 2009; Fujiwara & Hutchinson, 2012). The humerus and ulna share complementary articular surfaces and are connected by numerous muscles (*m. anconeus* and flexor and extensor muscles of the carpals and digits) and a strong joint cap (Barone, 2010a; Etienne *et al.*, 2021). Consequently, the humerus and ulna are strongly integrated among quadrupeds, i.e. they show a noticeable shape covariation (Fabre *et al.*, 2014; Martín-Serra *et al.*, 2015; Hanot *et al.*, 2017; Botton-Divet *et al.*, 2018), notably among modern rhinos (Mallet *et al.*, 2020). Our results indicate that this covariation is likely to concern mainly the distal part of the humerus and the proximal part of the ulna, leading to consider the elbow as a

probable modular structure among Rhinocerotoidea, i.e. an anatomical unit covarying more in itself than with other units (Klingenberg, 2008). Beyond purely functional requirements, this potential modularity can also be related to an evolutionary covariation of size, mass and gracility among Rhinocerotoidea. Similar observations have been highlighted in small carnivorans (Fabre *et al.*, 2014) and this assertion yet remains to be tested on modern and fossil rhinocerotoids through modularity tests (Goswami & Polly, 2010).

Bone shape and phylogenetic relationships

In addition to functional requirements, the evolutionary legacy between species has a strong but unequally distributed influence on the shape variation of the forelimb. Shape, size, mass and the degree of brachypody all carry a strong phylogenetic signal underlining that their variation is constrained by historical factors (Cubo, 2004). This influence is particularly visible on the humerus: most of the considered groups display a marked shape homogeneity despite variation in body proportions. This is not the case for the radius and the ulna, where the different groups are split depending more on their mass or degree of brachypody rather than their phylogenetic affinities. This is coherent with previous results on modern rhinos indicating that the shape of the stylopodium is more related to the phylogeny than that of the zeugopodium (Mallet *et al.*, 2019, 2020). This pattern seems to occur at the level of the whole superfamily, in accordance with the hypothesis of an increase of variation of the limb elements along a proximo-distal gradient (Hallgrímsson *et al.*, 2002; Young & Hallgrímsson, 2005).

However, one particular group does not seem to follow this general trend. While being closely related to stem clades like Hyracodontidae, giant Paraceratheriidae exhibit a humeral shape close to that of more derived groups like Aceratheriini. Marked shape changes relatively to the shape displayed by Hyracodontidae or Hyrachyidae are observable on the humerus. Conversely, the shapes of the radius and ulna (except for the proximal part of the latter) appear to retain a plesiomorphic condition close to that of small Hyrachyidae and Hyracodontidae, these bones displaying little morphological changes except their striking relative size. These observations underline the particularity of this group among Rhinocerotoidea, whose unique body shape has puzzled biologists since their discovery (Granger & Gregory, 1936; Fortelius & Kappelman, 1993; Prothero, 2013). These considerations appear contradictory with our previous findings indicating that the radius shape is strongly related to the degree of brachypody and poorly to phylogeny (and conversely for the humerus). It is possible that Paraceratheriidae underwent particular developmental processes constraining the zeugopodium shape, while the stylopodium was subject to marked morphological changes to ensure its role in body support and propulsion, constituting a unique pattern within the

superfamily. Ecological factors may also have a role in shaping the forelimb of Paraceratheriidae but this question remains to be addressed in a dedicated study.

Two other groups show marked differences with the common trend of shape variation among Rhinocerotoidea: Rhinocerotini. Species belonging to Teleoceratina like *Teleoceras* show a high degree of brachypody and their forelimb bones often display an extreme shape relatively to the whole superfamily, particularly on the zeugopodium. Their extreme brachypody had sometimes been associated with a semi-aquatic ecology, although this hypothesis is now considered unlikely (MacFadden, 1998; Mead, 2000; Mihlbachler, 2003; Prothero, 2005; Clementz, Holroyd, & Koch, 2008; Wang & Secord, 2020). Nevertheless, the extreme limb bone variation observed in *Teleoceras*, *Prosantorhinus*, and *Brachypotherium*, and their high abundance in Miocene fluvio-lacustrine settings with respect to coeval rhinos is compatible with that of semi-aquatic hippos (Antoine, pers. comm.) (Harrison & Manning, 1983; Wermelinger, 1998; Antoine, 2002; Hullot & Antoine, 2020). Despite the unique limb morphology of Teleoceratina, our results highlight many shape resemblances with fully terrestrial Aceratheriini (*Aphelops*, *Peraceras*) and Rhinocerotina (*Coelodonta*) and do not support the hypothesis of a semi-aquatic ecology either. A morphofunctional analysis focused on this subtribe could help to understand the factors driving this particular limb construction.

Finally, Rhinocerotina (i.e., the subtribe encompassing all living rhinoceroses) display a high shape homogeneity, particularly on the humerus and the ulna, despite a broad range of body mass and body proportions. The range of shape variation within this subtribe appears thus highly constrained by the evolutionary history. The ecological preferences encountered in Rhinocerotina do not seem to strongly impact the shape variation (Guérin, 1980; Cerdeño, 1998). However, this relative homogeneity relatively to the whole superfamily likely encompasses different trends of shape variation between genera that remain to be explored in detail.

CONCLUSION

The relations between shape variation of the forelimb bones, body proportions and phylogeny among Rhinocerotoidea vary but general trends are clearly observed despite this complexity. A common trend to the whole superfamily is the increase of bone robustness towards a higher body mass and higher degree of brachypody. The reinforcement of the insertions for the extensor muscles enables the animals to counteract the gravitational constraints when body mass increases. However, strong differences in shape variation exist between the stylopodium and the zeugopodium. The shape of the humerus modifies following size, mass and brachypody in a similar way within the whole superfamily, while being also strongly constrained by the evolutionary history. Conversely, the shape of the zeugopodium appears mostly associated to the degree of brachypody, namely the distribution of mass within the body (centre of gravity), rather than to the absolute mass itself. Surprisingly, the shape variation of bones in the elbow caudal region shows striking similarities, suggesting a likely modular organisation of the humerus and ulna. Beyond these general trends, groups like Paraceratheriidae, Teleoceratina and Rhinocerotina display divergent patterns that remain to be fully understood. Consequently, this exploration of the forelimb shape among Rhinocerotoidea encourages the application of the same morphofunctional approach on the hind limb to highlight how shape patterns converge or diverge between limbs under a similar weight constraint.

ACKNOWLEDGMENTS

The authors would like to warmly thank all the curators of the visited institutions for granting us access to the studied specimens: E. Hoeger, S. Ketelsen, R. O'Leary and J. Meng (American Museum of Natural History, New York, USA), J.-M. Pouillon and C. Bouix (Association Rhinopolis, Gannat, France), G. Rößner (Bayerische Staatssammlung für Paläontologie und Geologie, Munich, Germany), D. Berthet (Centre de Conservation et d'Étude des Collections, Musée des Confluences, Lyon, France), E. Robert (Collections de Géologie de Lyon, Université Lyon 1 Claude Bernard, Lyon, France), Yves Laurent (Muséum d'Histoire Naturelle de Toulouse, Toulouse, France), J. Lesur, A. Verguin (Muséum National d'Histoire Naturelle, Paris, France), R. Portela-Miguez, P. Brewer and R. Pappa (Natural History Museum, London, UK), L. Costeur and F. Dammeyer (Naturhistorisches Museum Basel, Basel, Switzerland), A. Folie, C. Cousin, O. Pauwels and S. Bruaux (Royal Belgian Institute of Natural Sciences, Brussels, Belgium), E. Gilissen (Royal Museum for Central Africa, Tervuren, Belgium) and D. Brinkman (Yale Peabody Museum, New Haven, CT, USA). We would also like to thanks W. Liu from the Institute of Vertebrate Paleontology and Paleoanthropology (Beijing, China), for providing a 3D model of *Juxia*, M. C. Reyes from the National Museum of the Philippines (Manila, Philippines) and T. Ingicco from the MNHN (Paris, France) for providing the 3D models of *N. philippinensis*, and J. Hutchinson from the Royal Veterinary College (London, UK) for providing us CT-scan data coming from the University of California Museum of Paleontology (Berkeley, USA). We are grateful to S. Castiglione and P. Raia (University of Naples Federico II, Naples, Italy) for their precious help in using the RRphylo package. Many thanks to K. Gaignebet and C. Bouquet for their help in reconstructing many 3D models. C.M. acknowledges C. Etienne, R. Lefebvre and R. Pintore (MNHN, Paris, France) for constructive discussions and advices on R programming, data analyses and interpretations. This work was funded by the European Research Council and is part of the GRAVIBONE project (ERC-2016-STG-715300).

AUTHOR CONTRIBUTIONS

C.M. designed the study with significant inputs from A.H., R.C. and G.B. C.M. did the data acquisition with inputs from A.H. C.M. performed the analyses with the help of R.C and G.B. and all authors interpreted the results. C.M. drafted the manuscript. All authors reviewed and contributed to the final version of the manuscript, read it and approved it.

DATA AVAILABILITY

The data underlying this article will be shared on reasonable request to the corresponding author.

REFERENCES

3D Systems Corporation. 2014. *Geomagic Studio*. 3D Systems Corporation.

Adams DC. 2014. A generalized K statistic for estimating phylogenetic signal from shape and other high-dimensional multivariate data. *Systematic Biology* 63: 685–697.

Adams DC, Collyer ML. 2018. Multivariate Phylogenetic Comparative Methods: Evaluations, Comparisons, and Recommendations. *Systematic Biology* 67: 14–31.

Adams DC, Otárola-Castillo E. 2013. geomorph: an r package for the collection and analysis of geometric morphometric shape data. *Methods in Ecology and Evolution* 4: 393–399.

Adams DC, Rohlf FJ, Slice DE. 2004. Geometric morphometrics: Ten years of progress following the 'revolution'. *Italian Journal of Zoology* 71: 5–16.

Agisoft. 2018. *PhotoScan Professional Edition*. Agisoft.

Alexander RM, Jayes AS, Maloiy GMO, Wathuta EM. 1979. Allometry of the limb bones of mammals from shrews (*Sorex*) to elephant (*Loxodonta*). *Journal of Zoology* 189: 305–314.

Antoine P-O. 2002. Phylogénie et évolution des Elasmotheriina (Mammalia, Rhinocerotidae). *Mémoires du Muséum National d'Histoire Naturelle (1993)* 188: 5–350.

Antoine P-O, Downing KF, Crochet J-Y, Duranthon F, Flynn LJ, Marivaux L, Métais G, Rajpar AR, Roohi G. 2010. A revision of *Aceratherium blanfordi* Lydekker, 1884 (Mammalia: Rhinocerotidae) from the Early Miocene of Pakistan: postcranials as a key. *Zoological Journal of the Linnean Society* 160: 139–194.

Antoine P-O, Duranthon F, Welcomme J-L. 2003. *Alicornops* (Mammalia, Rhinocerotidae) dans le Miocène supérieur des Collines Bugti (Balouchistan, Pakistan): implications phylogénétiques. *Geodiversitas* 25: 575–603.

Antoine P-O, Reyes MC, Amano N, Bautista AP, Chang CH, Claude J, De Vos J, Ingicco T. 2021. A new rhinoceros clade from the Pleistocene of Asia sheds light on mammal dispersals to the Philippines. *Zoological Journal of the Linnean Society*.

Arambourg C. 1959. Vertébrés continentaux du Miocène supérieur de l'Afrique du Nord. *Publications du Service de la Carte Géologique de l'Algérie (Nouvelle Série), Paléontologie, Mémoire, Serv. de la Carte Géol. de l'Algérie* 4: 1–161.

Artec 3D. 2018. *Artec Studio Professional*. Artec 3D.

Averianov A, Danilov I, Jin J, Wang Y. 2017. A new amynodontid from the Eocene of South China and phylogeny of Amynodontidae (Perissodactyla: Rhinocerotoidea). *Journal of Systematic Palaeontology* 15: 927–945.

Bai B, Meng J, Wang YQ, Wang HB, Holbrook L. 2017. Osteology of The Middle Eocene Ceratomorph *Hyrachyus modestus* (Mammalia, Perissodactyla). *Bulletin of the American Museum of Natural History*: 1–70.

911 Bai B, Meng J, Zhang C, Gong YX, Wang YQ. 2020. The origin of Rhinocerotoidea and
912 phylogeny of Ceratomorpha (Mammalia, Perissodactyla). *Communications Biology* 3: 1–16.

913 Baker J, Meade A, Pagel M, Venditti C. 2015. Adaptive evolution toward larger size in
914 mammals. *Proceedings of the National Academy of Sciences* 112: 5093–5098.

915 Bardua C, Felice RN, Watanabe A, Fabre A-C, Goswami A. 2019. A Practical Guide to Sliding
916 and Surface Semilandmarks in Morphometric Analyses. *Integrative Organismal Biology* 1: 1–
917 34.

918 Barone R. 2010a. *Anatomie comparée des mammifères domestiques. Tome 1 : Ostéologie*.
919 Paris: Vigot Frères.

920 Barone R. 2010b. *Anatomie comparée des mammifères domestiques. Tome 2 : Arthrologie et*
921 *myologie*. Paris: Vigot Frères.

922 Baylac M, Frieß M. 2005. Fourier Descriptors, Procrustes Superimposition, and Data
923 Dimensionality: An Example of Cranial Shape Analysis in Modern Human Populations. In:
924 Slice DE, ed. *Developments in Primatology: Progress and Prospects*. *Modern Morphometrics*
925 *in Physical Anthropology*. Boston, MA: Springer US, 145–165.

926 Becker D. 2003. Paléoécologie et paléoclimats de la molasse du Jura (oligo-miocène).
927 Unpublished thesis, Université de Fribourg.

928 Becker D, Antoine P-O, Maridet O. 2013. A new genus of Rhinocerotidae (Mammalia,
929 Perissodactyla) from the Oligocene of Europe. *Journal of Systematic Palaeontology* 11: 947–
930 972.

931 Becker D, Bürgin T, Oberli U, Scherler L. 2009. *Diaceratherium lemanense* (Rhinocerotidae)
932 from Eschenbach (eastern Switzerland): systematics, palaeoecology, palaeobiogeography.
933 *Neues Jahrbuch für Geologie und Paläontologie-Abhandlungen* 254: 5–39.

934 Bertram JEA, Biewener AA. 1990. Differential scaling of the long bones in the terrestrial
935 carnivora and other mammals. *Journal of Morphology* 204: 157–169.

936 Bertram JEA, Biewener AA. 1992. Allometry and curvature in the long bones of quadrupedal
937 mammals. *Journal of Zoology* 226: 455–467.

938 Biasatti D, Wang Y, Deng T. 2018. Paleoecology of Cenozoic rhinos from northwest China: a
939 stable isotope perspective. *Vertebrata PalAsiatica* 56: 45–68.

940 Biewener AA. 1989a. Mammalian Terrestrial Locomotion and Size. *BioScience* 39: 776–783.

941 Biewener AA. 1989b. Scaling body support in mammals: limb posture and muscle mechanics.
942 *Science* 245: 45–48.

943 Biewener AA, Patek SN. 2018. *Animal locomotion*. New York: Oxford University Press.

944 Blomberg SP, Garland T, Ives AR, Crespi B. 2003. Testing for phylogenetic signal in
945 comparative data: behavioral traits are more labile. *Evolution* 57: 717–745.

946 Boada-Saña A. 2008. Phylogénie du rhinocérotidé *Diaceratherium* Dietrich, 1931 (Mammalia,
947 Perissodactyla).

948 Bokma F, Godinot M, Maridet O, Ladevèze S, Costeur L, Solé F, Gheerbrant E, Peigné S,
949 Jacques F, Laurin M. 2016. Testing for Depéret's Rule (Body Size Increase) in Mammals using
950 Combined Extinct and Extant Data. *Systematic Biology* 65: 98–108.

951 Botton-Divet L, Cornette R, Fabre A-C, Herrel A, Houssaye A. 2016. Morphological Analysis of
952 Long Bones in Semi-aquatic Mustelids and their Terrestrial Relatives. *Integrative and*
953 *Comparative Biology* 56: 1298–1309.

954 Botton-Divet L, Cornette R, Houssaye A, Fabre A-C, Herrel A. 2017. Swimming and running: a
955 study of the convergence in long bone morphology among semi-aquatic mustelids
956 (Carnivora: Mustelidae). *Biological Journal of the Linnean Society* 121: 38–49.

957 Botton-Divet L, Houssaye A, Herrel A, Fabre A-C, Cornette R. 2018. Swimmers, Diggers,
958 Climbers and More, a Study of Integration Across the Mustelids' Locomotor Apparatus
959 (Carnivora: Mustelidae). *Evolutionary Biology* 45: 182–195.

960 Cappellini E, Welker F, Pandolfi L, Ramos-Madrigal J, Samodova D, Rüther PL, Fotakis AK,
961 Lyon D, Moreno-Mayar JV, Bukhsianidze M, Jersie-Christensen RR, Mackie M, Ginolhac A,
962 Ferring R, Tappen M, Palkopoulou E, Dickinson MR, Stafford TW, Chan YL, Götherström A,
963 Nathan SKSS, Heintzman PD, Kapp JD, Kirillova I, Moodley Y, Agusti J, Kahlke RD, Kiladze G,
964 Martínez-Navarro B, Liu S, Velasco MS, Sinding MHS, Kelstrup CD, Allentoft ME, Orlando L,
965 Penkman K, Shapiro B, Rook L, Dalén L, Gilbert MTP, Olsen JV, Lordkipanidze D, Willerslev E.
966 2019. Early Pleistocene enamel proteome from Dmanisi resolves *Stephanorhinus* phylogeny.
967 *Nature* 574: 103–107.

968 Carrano MT. 1999. What, if anything, is a cursor? Categories versus continua for determining
969 locomotor habit in mammals and dinosaurs. *Journal of Zoology* 247: 29–42.

970 Cassini GH, Vizcaíno SF, Bargo MS. 2012. Body mass estimation in Early Miocene native
971 South American ungulates: a predictive equation based on 3D landmarks. *Journal of Zoology*
972 287: 53–64.

973 Castiglione S, Tesone G, Piccolo M, Melchionna M, Mondanaro A, Serio C, Febbraro MD, Raia
974 P. 2018. A new method for testing evolutionary rate variation and shifts in phenotypic
975 evolution. *Methods in Ecology and Evolution* 9: 974–983.

976 Cerdeño E. 1995. Cladistic analysis of the family Rhinocerotidae (Perissodactyla). *American*
977 *Museum novitates* 3143: 1–25.

978 Cerdeño E. 1998. Diversity and evolutionary trends of the Family Rhinocerotidae
979 (Perissodactyla). *Palaeogeography, Palaeoclimatology, Palaeoecology* 141: 13–34.

980 Chen S, Deng T, Hou S, Shi Q, Pang L. 2010. Sexual Dimorphism in Perissodactyl Rhinocerotid
981 *Chilotherium wimani* from the Late Miocene of the Linxia Basin (Gansu, China). *Acta*
982 *Palaeontologica Polonica* 55: 587–597.

983 Cignoni P, Callieri M, Corsini M, Dellepiane M, Ganovelli F, Ranzuglia G. 2008. *MeshLab: an*
984 *Open-Source Mesh Processing Tool*. The Eurographics Association.

985 Colbert EH. 1938. Fossil mammals from Burma in the American Museum of Natural History.
986 *Bulletin of the American Museum of Natural History* 74: 255–436.

987 Coombs WP. 1978. Theoretical Aspects of Cursorial Adaptations in Dinosaurs. *The Quarterly*
988 *Review of Biology* 53: 393–418.

989 Cope ED. 1887. *The origin of the fittest: Essays on evolution*. New York: Appleton.

990 Coughlin BL, Fish FE. 2009. Hippopotamus Underwater Locomotion: Reduced-Gravity
991 Movements for a Massive Mammal. *Journal of Mammalogy* 90: 675–679.

992 Cubo J. 2004. Pattern and process in constructional morphology. *Evolution & Development* 6:
993 131–133.

994 Depéret C. 1907. *Les transformations du monde animal*. Paris: Flammarion.

995 Dinerstein E. 1991. Sexual Dimorphism in the Greater One-Horned Rhinoceros (*Rhinoceros*
996 *unicornis*). *Journal of Mammalogy* 72: 450–457.

997 Dinerstein E. 2011. Family Rhinocerotidae (Rhinoceroses). In: Wilson DE, Mittermeier RA,
998 eds. *Handbook of the Mammals of the World*. Barcelona: Don E. Wilson & Russel A.
999 Mittermeier, 144–181.

1000 Dutto DJ, Hoyt DF, Clayton HM, Cogger EA, Wickler SJ. 2006. Joint work and power for both
1001 the forelimb and hindlimb during trotting in the horse. *Journal of Experimental Biology* 209:
1002 3990–3999.

1003 Eisenmann V, Guérin C. 1984. Morphologie fonctionnelle et environnement chez les
1004 périssodactyles. *Geobios* 17: 69–74.

1005 Ercoli MD, Prevosti FJ. 2011. Estimación de Masa de las Especies de Sparassodonta
1006 (Mammalia, Metatheria) de Edad Santacrucense (Mioceno Temprano) a Partir del Tamaño
1007 del Centroide de los Elementos Apendiculares: Inferencias Paleoecológicas. *Ameghiniana* 48:
1008 462–479.

1009 Etienne C, Houssaye A, Hutchinson JR. 2021. Limb myology and muscle architecture of the
1010 Indian rhinoceros *Rhinoceros unicornis* and the white rhinoceros *Ceratotherium simum*
1011 (Mammalia: Rhinocerotidae). *PeerJ* 9: e11314.

1012 Etienne C, Mallet C, Cornette R, Houssaye A. 2020. Influence of mass on tarsus shape
1013 variation: a morphometrical investigation among Rhinocerotidae (Mammalia:
1014 Perissodactyla). *Biological Journal of the Linnean Society* 129: 950–974.

1015 Fabre A-C, Goswami A, Peigné S, Cornette R. 2014. Morphological integration in the forelimb
1016 of musteloid carnivorans. *Journal of Anatomy* 225: 19–30.

1017 Fau M, Cornette R, Houssaye A. 2016. Photogrammetry for 3D digitizing bones of mounted
1018 skeletons: Potential and limits. *Comptes Rendus Palevol* 15: 968–977.

1019 Federative Committee on Anatomical Terminology. 1998. *Terminologia Anatomica*. Georg
1020 Thieme Verlag.

1021 Felsenstein J. 1985. Phylogenies and the Comparative Method. *The American Naturalist* 125:
1022 1–15.

1023 Felsenstein J. 2004. *Inferring Phylogenies*. Sunderland, Mass: OUP USA.

1024 Fernando P, Polet G, Foead N, Ng LS, Pastorini J, Melnick DJ. 2006. Genetic diversity,
1025 phylogeny and conservation of the Javan rhinoceros (*Rhinoceros sondaicus*). *Conservation*
1026 *Genetics* 7: 439–448.

1027 Fisher RE, Scott KM, Naples VL. 2007. Forelimb myology of the pygmy hippopotamus
1028 (*Choeropsis liberiensis*). *The Anatomical Record* 290: 673–693.

1029 Fortelius M, Kappelman J. 1993. The largest land mammal ever imagined. *Zoological Journal*
1030 *of the Linnean Society* 108: 85–101.

1031 Fujiwara S. 2009. Olecranon orientation as an indicator of elbow joint angle in the stance
1032 phase, and estimation of forelimb posture in extinct quadruped animals. *Journal of*
1033 *Morphology* 270: 1107–1121.

1034 Fujiwara S, Hutchinson JR. 2012. Elbow joint adductor moment arm as an indicator of
1035 forelimb posture in extinct quadrupedal tetrapods. *Proceedings of the Royal Society of*
1036 *London B: Biological Sciences* 279: 2561–2570.

1037 Gaudry M. 2017. Molecular phylogenetics of the rhinoceros clade and evolution of UCP1
1038 transcriptional regulatory elements across the mammalian phylogeny. Unpublished thesis,
1039 University of Manitoba.

1040 Goolsby EW. 2015. Phylogenetic Comparative Methods for Evaluating the Evolutionary
1041 History of Function-Valued Traits. *Systematic Biology* 64: 568–578.

1042 Goswami A, Polly PD. 2010. Methods for Studying Morphological Integration and Modularity.
1043 *The Paleontological Society Papers* 16: 213–243.

1044 Gower JC. 1975. Generalized procrustes analysis. *Psychometrika* 40: 33–51.

1045 Granger W, Gregory WK. 1936. Further notes on the gigantic extinct rhinoceros,
1046 Baluchitherium, from the Oligocene of Mongolia. *Bulletin of the American Museum of*
1047 *Natural History* 72: 1–73.

1048 Gregory WK. 1912. Notes on the Principles of Quadrupedal Locomotion and on the
1049 Mechanism of the Limbs in Hoofed Animals. *Annals of the New York Academy of Sciences* 22:
1050 267–294.

1051 Guérin C. 1980. Les Rhinocéros (Mammalia, Perissodactyla) du Miocène terminal au
1052 Pléistocène supérieur en Europe occidentale. Comparaison avec les espèces actuelles.

1053 Guérin C. 1989. La famille des Rhinocerotidae (Mammalia, Perissodactyla) : systématique,
1054 histoire, évolution, paléoécologie. *Cranium* 6: 3–14.

1055 Gunz P, Mitteroecker P. 2013. Semilandmarks: a method for quantifying curves and surfaces.
1056 *Hystrix, the Italian Journal of Mammalogy* 24: 103–109.

1057 Gunz P, Mitteroecker P, Bookstein FL. 2005. Semilandmarks in Three Dimensions. In: Slice
1058 DE, ed. *Developments in Primatology: Progress and Prospects*. *Modern Morphometrics in*
1059 *Physical Anthropology*. Boston, MA: Slice, D. E., 73–98.

1060 Hallgrímsson B, Katz DC, Aponte JD, Larson JR, Devine J, Gonzalez PN, Young NM, Roseman
1061 CC, Marcucio RS. 2019. Integration and the Developmental Genetics of Allometry.
1062 *Integrative and Comparative Biology* 59: 1369–1381.

1063 Hallgrímsson B, Willmore K, Hall BK. 2002. Canalization, developmental stability, and
1064 morphological integration in primate limbs. *American Journal of Physical Anthropology* 119:
1065 131–158.

1066 Hanot P, Herrel A, Guintard C, Cornette R. 2017. Morphological integration in the
1067 appendicular skeleton of two domestic taxa: the horse and donkey. *Proc. R. Soc. B* 284:
1068 20171241.

1069 Harrison JA, Manning EM. 1983. Extreme carpal variability in *Teleoceras* (Rhinocerotidae,
1070 Mammalia). *Journal of Vertebrate Paleontology* 3: 58–64.

1071 Heissig K. 2012. Les Rhinocerotidae (Perissodactyla) de Sansan. In: Peigné S, Sen S, eds.
1072 *Mémoires du Muséum national d'histoire naturelle*. *Mammifères de Sansan*. Paris, 317–485.

1073 Henderson DM. 2006. Burly gaits: centers of mass, stability, and the trackways of sauropod
1074 dinosaurs. *Journal of Vertebrate Paleontology* 26: 907–921.

1075 Henderson K, Pantinople J, McCabe K, Richards HL, Milne N. 2017. Forelimb bone curvature
1076 in terrestrial and arboreal mammals. *PeerJ* 5: e3229.

1077 Hermanson JW, MacFadden BJ. 1992. Evolutionary and functional morphology of the
1078 shoulder region and stay-apparatus in fossil and extant horses (Equidae). *Journal of*
1079 *Vertebrate Paleontology* 12: 377–386.

1080 Hildebrand M. 1974. *Analysis of vertebrate structure*. New York: John Wiley & Sons.

1081 Ho J, Tumkaya T, Aryal S, Choi H, Claridge-Chang A. 2019. Moving beyond P values: data
1082 analysis with estimation graphics. *Nature Methods* 16: 565–566.

1083 Houssaye A, Fernandez V, Billet G. 2016. Hyperspecialization in Some South American
1084 Endemic Ungulates Revealed by Long Bone Microstructure. *Journal of Mammalian Evolution*
1085 23: 221–235.

1086 Hullot M, Antoine P-O. 2020. Mortality curves and population structures of late early
1087 Miocene Rhinocerotidae (Mammalia, Perissodactyla) remains from the Béon 1 locality of
1088 Montréal-du-Gers, France. *Palaeogeography, Palaeoclimatology, Palaeoecology*: 109938.

1089 Jenkins FA. 1973. The functional anatomy and evolution of the mammalian humero-ulnar
1090 articulation. *American Journal of Anatomy* 137: 281–297.

1091 Klingenberg CP. 2008. Morphological Integration and Developmental Modularity. *Annual*
1092 *Review of Ecology, Evolution, and Systematics* 39: 115–132.

1093 Klingenberg CP. 2014. Studying morphological integration and modularity at multiple levels:
1094 concepts and analysis. *Philosophical Transactions of the Royal Society B: Biological Sciences*
1095 369: 20130249.

1096 Klingenberg CP. 2016. Size, shape, and form: concepts of allometry in geometric
1097 morphometrics. *Development Genes and Evolution* 226: 113–137.

1098 Klingenberg CP, Marugán-Lobón J. 2013. Evolutionary Covariation in Geometric
1099 Morphometric Data: Analyzing Integration, Modularity, and Allometry in a Phylogenetic
1100 Context. *Systematic Biology* 62: 591–610.

1101 Larramendi A. 2016. Shoulder height, body mass and shape of proboscideans. *Acta*
1102 *Palaeontologica Polonica* 61: 537–574.

1103 Lu X. 2013. A juvenile skull of *Acerorhinus yuanmouensis* (Mammalia: Rhinocerotidae) from
1104 the Late Miocene hominoid fauna of the Yuanmou Basin (Yunnan, China). *Geobios* 46: 539–
1105 548.

1106 Mallet C, Billet G, Houssaye A, Cornette R. 2020. A first glimpse at the influence of body mass
1107 in the morphological integration of the limb long bones: an investigation in modern
1108 rhinoceroses. *Journal of Anatomy* 237: 704–726.

1109 Mallet C, Cornette R, Billet G, Houssaye A. 2019. Interspecific variation in the limb long
1110 bones among modern rhinoceroses—extent and drivers. *PeerJ* 7: e7647.

1111 Mallison H, Wings O. 2014. Photogrammetry in Paleontology - A practical guide. *Journal of*
1112 *Paleontological Techniques*: 1–31.

1113 Martins EP, Hansen TF. 1997. Phylogenies and the Comparative Method: A General
1114 Approach to Incorporating Phylogenetic Information into the Analysis of Interspecific Data.
1115 *The American Naturalist* 149: 646–667.

1116 Martín-Serra A, Figueirido B, Pérez-Claros JA, Palmqvist P. 2015. Patterns of morphological
1117 integration in the appendicular skeleton of mammalian carnivores. *Evolution* 69: 321–340.

1118 Mead AJ. 2000. Sexual dimorphism and paleoecology in *Teleoceras*, a North American
1119 Miocene rhinoceros. *Paleobiology* 26: 689–706.

Mihlbachler MC. 2007. Sexual Dimorphism and Mortality Bias in a Small Miocene North American Rhino, *Menoceras arikarense*: Insights into the Coevolution of Sexual Dimorphism and Sociality in Rhinos. *Journal of Mammalian Evolution* 14: 217–238.

Milne N. 2016. Curved bones: An adaptation to habitual loading. *Journal of Theoretical Biology* 407: 18–24.

Mitteroecker P, Gunz P, Windhager S, Schaefer K. 2013. A brief review of shape, form, and allometry in geometric morphometrics, with applications to human facial morphology. *Hystrix, the Italian Journal of Mammalogy* 24: 59–66.

Orlando L, Leonard JA, Thenot A, Laudet V, Guerin C, Hänni C. 2003. Ancient DNA analysis reveals woolly rhino evolutionary relationships. *Molecular Phylogenetics and Evolution* 28: 485–499.

Osborn HF. 1929. *The Titanotheres of ancient Wyoming, Dakota, and Nebraska*. Government Printing Office.

Panagiotopoulou O, Pataky TC, Hutchinson JR. 2019. Foot pressure distribution in White Rhinoceroses (*Ceratotherium simum*) during walking. *PeerJ* 7: e6881.

Paradis E, Blomberg SP, Bolker B, Brown J, Claude J, Cuong HS, Desper R, Didier G, Durand B, Dutheil J, Ewing J, Gascuel O, Guillerme T, Heibl C, Ives A, Jones B, Krah F, Lawson D, Lefort V, Legendre P, Lemon J, Marcon E, McCloskey R, Nylander J, Opgen-Rhein R, Popescu AA, Royer-Carenzi M, Schliep K, Strimmer K, de Vienne D. 2018. *Ape: Analyses of Phylogenetics and Evolution*.

Piras P, Maiorino L, Raia P, Marcolini F, Salvi D, Vignoli L, Kotsakis T. 2010. Functional and phylogenetic constraints in Rhinocerotinae craniodental morphology. *Evolutionary Ecology Research* 12: 897–928.

Polly PD. 2007. Limbs in mammalian evolution. Chapter 15. In: Hall BK, ed. *Fins into Limbs: Evolution, Development, and Transformation*. Chicago: Brian K. Hall, 245–268.

Price SA, Bininda-Emonds ORP. 2009. A comprehensive phylogeny of extant horses, rhinos and tapirs (Perissodactyla) through data combination. *Zoosystematics and Evolution* 85: 277–292.

Prothero DR. 1998. Hyracodontidae. In: Janis CM, Scott KM, Jacobs LL, eds. *Evolution of Tertiary Mammals of North America: Volume 1, Terrestrial Carnivores, Ungulates, and Ungulate Like Mammals*. Cambridge University Press, 589–593.

Prothero DR. 2005. *The Evolution of North American Rhinoceroses*. Cambridge.

Prothero DR. 2013. *Rhinoceros Giants: The Paleobiology of Indricotheres*. Bloomington and Indianapolis.

Prothero DR, Schoch RM. 1989. *The evolution of perissodactyls*. New York: Oxford University Press.

1156 Prothero DR, Sereno PC. 1982. Allometry and Paleoecology of Medial Miocene Dwarf
1157 Rhinoceroses from the Texas Gulf Coastal Plain. *Paleobiology* 8: 16–30.

1158 Qiu ZX, Wang BY. 2007. Paracerathere Fossils of China. *Palaeontologia Sinica, newseries C*
1159 29: 1–396.

1160 R Core Team. 2014. *R: a language and environment for statistical computing*. Vienna: R
1161 Foundation for Statistical Computing.

1162 Raia P, Carotenuto F, Passaro F, Fulgione D, Fortelius M. 2012. Ecological Specialization in
1163 Fossil Mammals Explains Cope's Rule. *The American Naturalist* 179: 328–337.

1164 Regnault S, Hermes R, Hildebrandt T, Hutchinson J, Weller R. 2013. Osteopathology in the
1165 feet of rhinoceroses: lesion type and distribution. *Journal of Zoo and Wildlife Medicine* 44:
1166 918–927.

1167 Revell LJ. 2012. phytools: an R package for phylogenetic comparative biology (and other
1168 things). *Methods in Ecology and Evolution* 3: 217–223.

1169 Rohlf FJ. 2001. Comparative Methods for the Analysis of Continuous Variables: Geometric
1170 Interpretations. *Evolution* 55: 2143–2160.

1171 Rohlf FJ, Slice D. 1990. Extensions of the Procrustes Method for the Optimal Superimposition
1172 of Landmarks. *Systematic Biology* 39: 40–59.

1173 Scherler L, Mennecart B, Hiard F, Becker D. 2013. Evolutionary history of hoofed mammals
1174 during the Oligocene–Miocene transition in Western Europe. *Swiss Journal of Geosciences*
1175 106: 349–369.

1176 Schlager S. 2017. Chapter 9 - Morpho and Rvcg – Shape Analysis in R: R-Packages for
1177 Geometric Morphometrics, Shape Analysis and Surface Manipulations. In: Zheng G, Li S,
1178 Székely G, eds. *Statistical Shape and Deformation Analysis*. Academic Press, 217–256.

1179 Schliep KP. 2011. phangorn: phylogenetic analysis in R. *Bioinformatics* 27: 592–593.

1180 Serio C, Raia P, Meloro C. 2020. Locomotory Adaptations in 3D Humerus Geometry of
1181 Xenarthra: Testing for Convergence. *Frontiers in Ecology and Evolution* 8.

1182 Steiner CC, Ryder OA. 2011. Molecular phylogeny and evolution of the Perissodactyla.
1183 *Zoological Journal of the Linnean Society* 163: 1289–1303.

1184 Stilson KT, Hopkins SSB, Davis EB. 2016. Osteopathology in Rhinocerotidae from 50 Million
1185 Years to the Present. *PLOS ONE* 11: e0146221.

1186 Swenson N. 2014. *Functional and Phylogenetic Ecology in R*. New York: Springer-Verlag.

1187 Thermo Fisher Scientific. 2018. *Avizo*.

1188 Tissier J, Antoine P-O, Becker D. 2020. New material of *Epiaceratherium* and a new species of
1189 *Mesaceratherium* clear up the phylogeny of early Rhinocerotidae (Perissodactyla). *Royal*
1190 *Society Open Science* 7: 200633.

1191 Tissier J, Becker D, Codrea V, Costeur L, Fărcaş C, Solomon A, Venczel M, Maridet O. 2018.
1192 New data on Amynodontidae (Mammalia, Perissodactyla) from Eastern Europe: Phylogenetic
1193 and palaeobiogeographic implications around the Eocene-Oligocene transition. *PLOS ONE*
1194 13: e0193774.

1195 Tougard C, Delefosse T, Hänni C, Montgelard C. 2001. Phylogenetic Relationships of the Five
1196 Extant Rhinoceros Species (Rhinocerotidae, Perissodactyla) Based on Mitochondrial
1197 Cytochrome b and 12S rRNA Genes. *Molecular Phylogenetics and Evolution* 19: 34–44.

1198 Wang H, Bai B, Meng J, Wang Y. 2016. Earliest known unequivocal rhinocerotoid sheds new
1199 light on the origin of Giant Rhinos and phylogeny of early rhinocerotoids. *Scientific Reports* 6.

1200 Wasserstein RL, Schirm AL, Lazar NA. 2019. Moving to a World Beyond "p < 0.05". *The*
1201 *American Statistician* 73: 1–19.

1202 Watson JC, Wilson AM. 2007. Muscle architecture of biceps brachii, triceps brachii and
1203 supraspinatus in the horse. *Journal of Anatomy* 210: 32–40.

1204 Welker F, Smith GM, Hutson JM, Kindler L, Garcia-Moreno A, Villaluenga A, Turner E,
1205 Gaudzinski-Windheuser S. 2017. Middle Pleistocene protein sequences from the rhinoceros
1206 genus *Stephanorhinus* and the phylogeny of extant and extinct Middle/Late Pleistocene
1207 Rhinocerotidae. *PeerJ* 5: e3033.

1208 Wermelinger M. 1998. *Prosantorhinus* cf. *douvillei* (Mammalia, Rhinocerotidae), petit
1209 rhinocéros du gisement miocène (MN 4b) de Montréal-du-Gers (Gers, France). Etude
1210 ostéologique du membre thoracique. Unpublished thesis, Université de Toulouse.

1211 Wiley DF, Amenta N, Alcantara DA, Ghosh D, Kil YJ, Delson E, Harcourt-Smith W, Rohlf FJ, St.
1212 John K, Hamann B. 2005. Evolutionary Morphing. *Proceedings of IEEE Visualization 2005*.
1213 Minneapolis, Minnesota.

1214 Willerslev E, Gilbert MTP, Binladen J, Ho SY, Campos PF, Ratan A, Tomsho LP, da Fonseca RR,
1215 Sher A, Kuznetsova TV, Nowak-Kemp M, Roth TL, Miller W, Schuster SC. 2009. Analysis of
1216 complete mitochondrial genomes from extinct and extant rhinoceroses reveals lack of
1217 phylogenetic resolution. *BMC Evolutionary Biology* 9: 1–11.

1218 Young NM, Hallgrímsson B. 2005. Serial Homology and the Evolution of Mammalian Limb
1219 Covariation Structure. *Evolution* 59: 2691–2704.

1220 Yuan J, Sheng G, Hou X, Shuang X, Yi J, Yang H, Lai X. 2014. Ancient DNA sequences from
1221 *Coelodonta antiquitatis* in China reveal its divergence and phylogeny. *Science China Earth*
1222 *Sciences* 57: 388–396.

1223 Zelditch ML, Swiderski DL, Sheets HD, Fink WL. 2012. *Geometric morphometrics for*
1224 *biologists: A Primer*. Academic Press.

1225 Zschokke S, Baur B. 2002. Inbreeding, outbreeding, infant growth, and size dimorphism in
1226 captive Indian rhinoceros (*Rhinoceros unicornis*). *Canadian Journal of Zoology* 80: 2014–
1227 2023.

1228

1229

FIGURES

Figure 1. Composite cladogram of the studied species among Rhinocerotoidea (Mammalia, Perissodactyla). Families, subfamilies, tribes and subtribes are defined by a colour code following the cladistic framework of Antoine *et al.* (2003) and Becker *et al.* (2013). All silhouettes representing a member of each group are at scale (provided by www.phylopic.org under Creative Commons license).

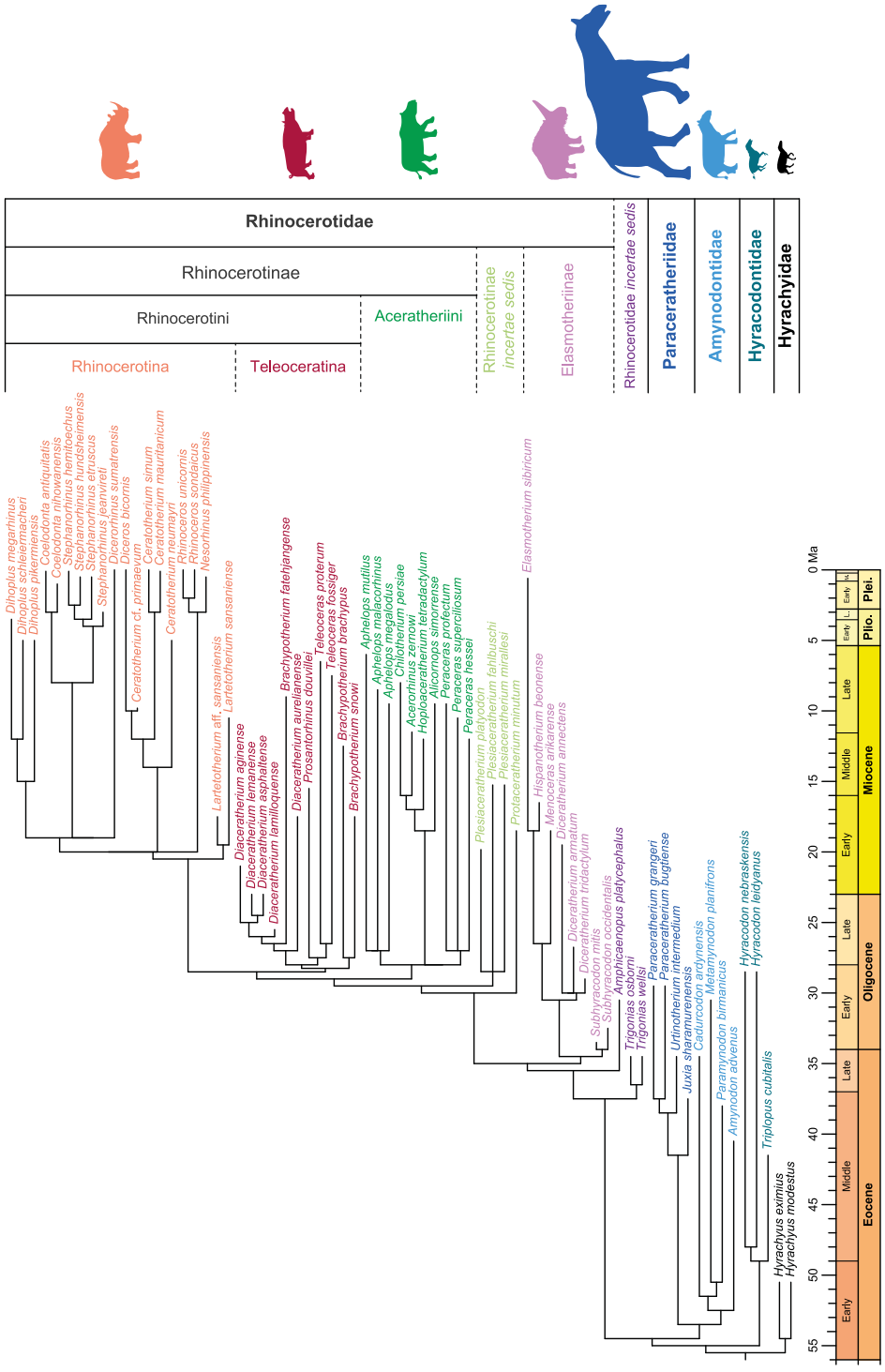

Figure 2. Evolution of BM and GI-MC3 along the phylogeny for the studied species within Rhinocerotoidea (Mammalia, Perissodactyla). Left: mean BM; Right: mean GI-MC3. Computations were made on log-transformed cubic root of mean BM (BM) and log-transformed GI-MC3. Values at nodes and along branches were reconstructed based on a Brownian motion model of evolution (Revell, 2012). Colour code for taxa follows Figure 1. Dashed lines indicate missing data. Evolution of the third metacarpal shape depending on the GI-MC3 value is illustrated by specimens *Hyrachyus modestus* AMNH FM 17436 (minimum) and *Teleoceras fossiger* AMNH FM 2636 (maximum).

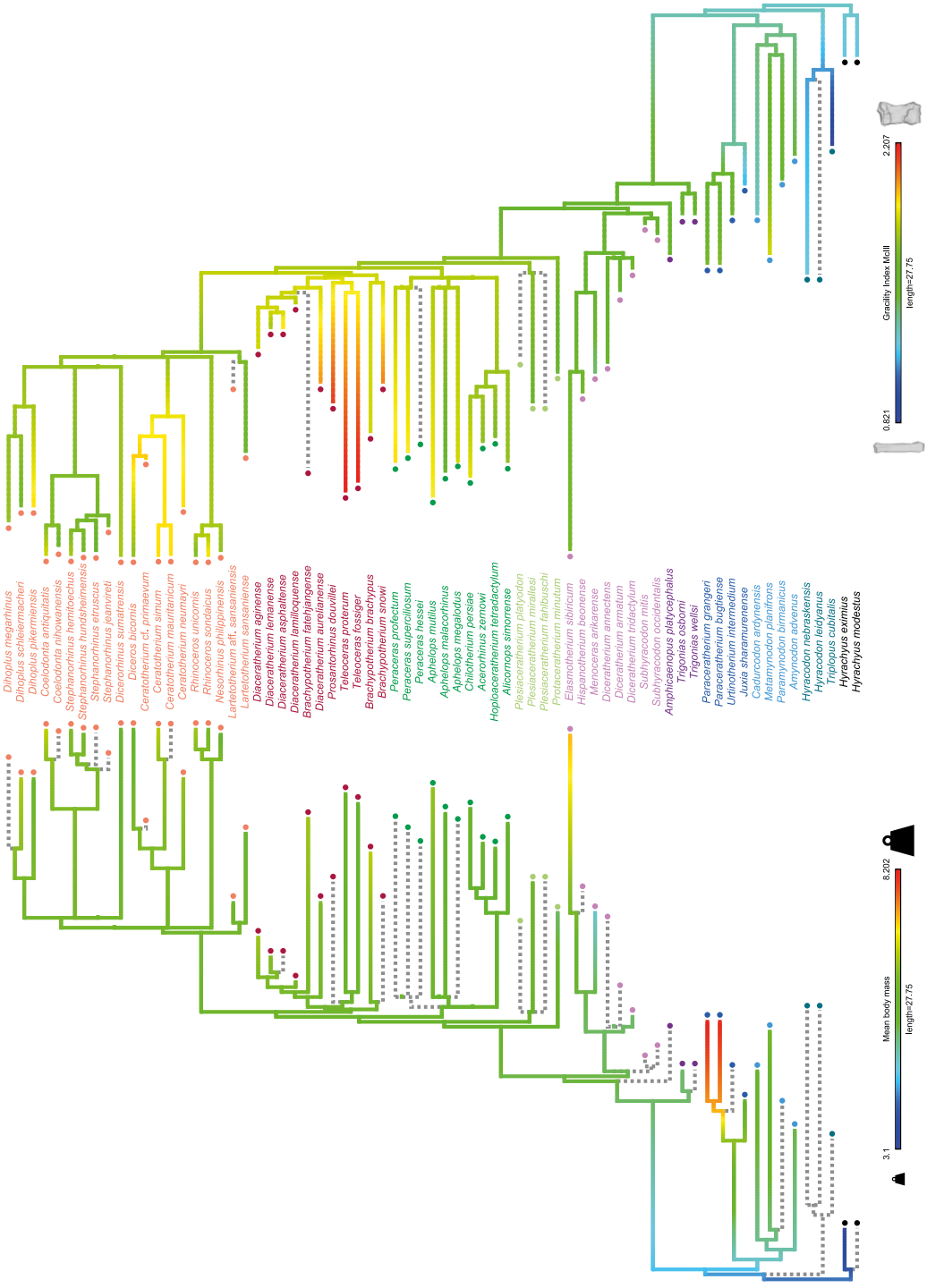

Figure 3. Neighbour Joining trees computed on all PC scores obtained from the PCAs performed on shape data. Colour code follows Figure 1 and abbreviations follow Table 1. Point size is proportional to the mean log centroid size of each species. **A:** complete humerus; **B**: distal partial humerus; **C:** radius; **D:** complete ulna; **E**: ulna without olecranon tuberosity; **F:** proximal partial ulna.

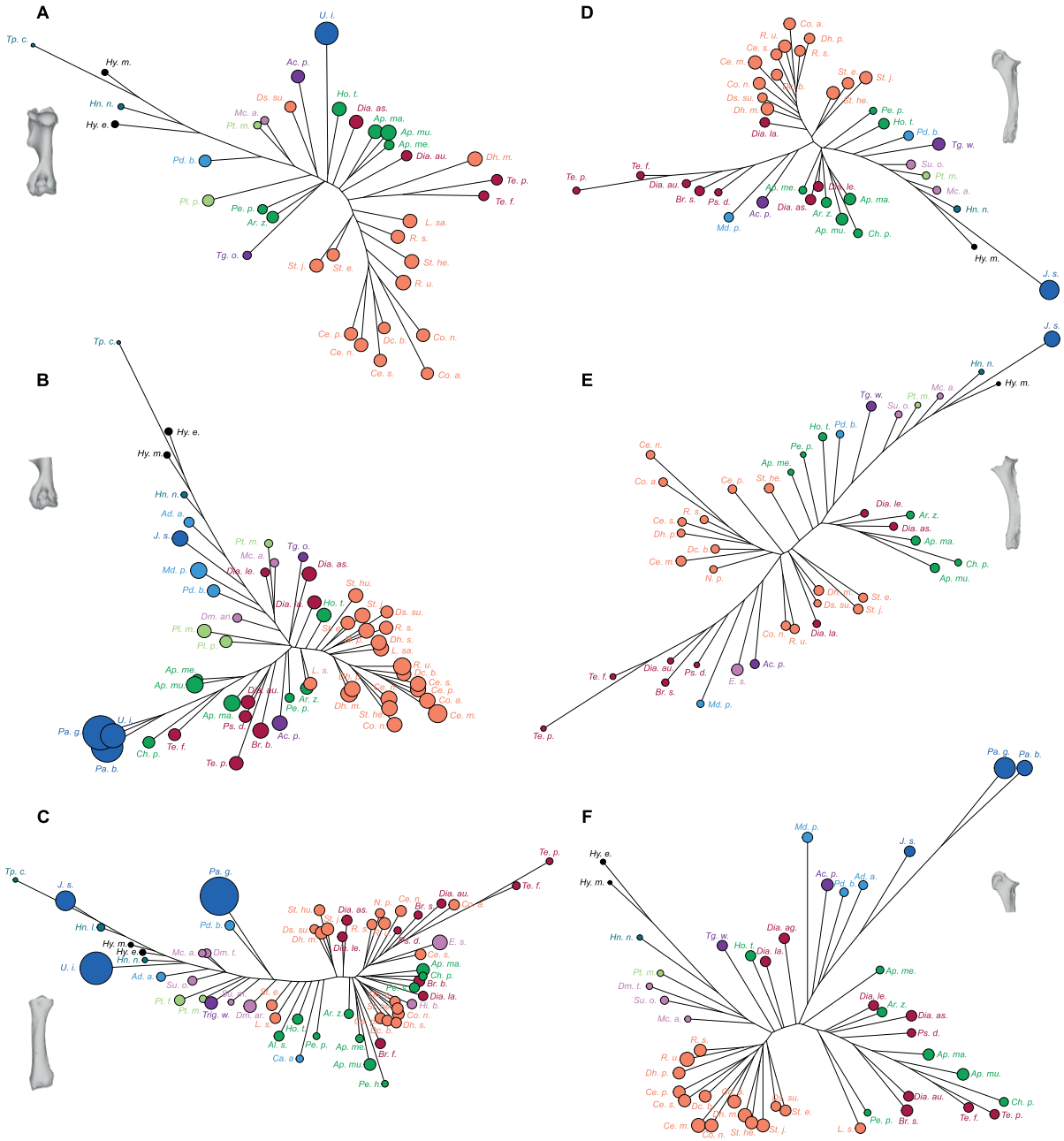

Figure 4. Results of the PCA performed on morphometric data of complete humerus (**A**) and distal partial humerus (**B**) and shape variation associated with the first two axes of the PCA (caudal view). Blue: negative side of the axis. Orange: positive side of the axis. Phylogenetic relationships are

plotted in the morphospace. Colour code follows Figure 1 and abbreviations follow Table 1. Point size is proportional to the centroid size of each species.

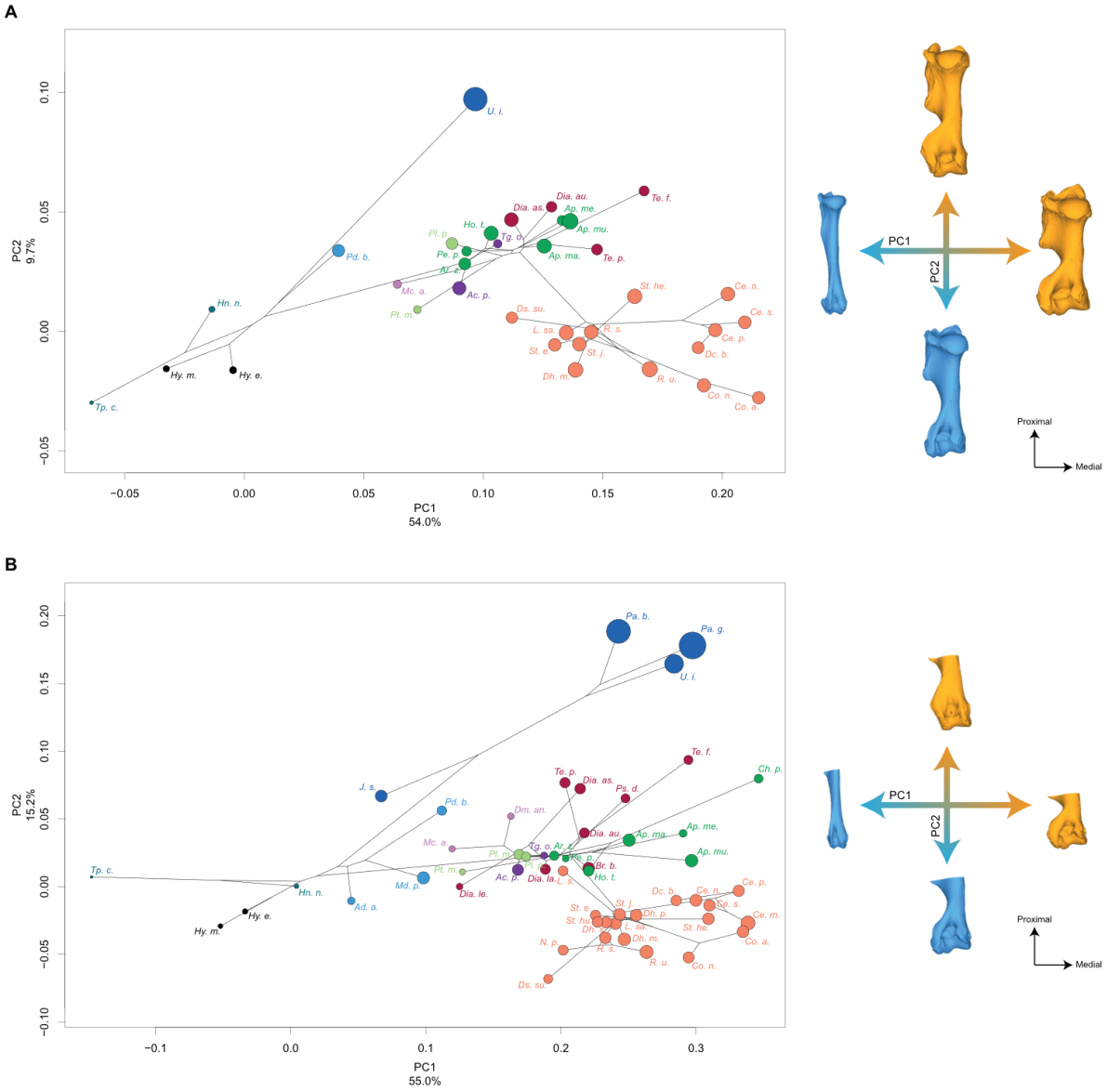

Figure 5. Significant PGLS regression plots for complete humerus performed on shape data and log-transformed centroid size (CS) (**A**), log-transformed cubic root of mean body mass (BM) (**B**), log-transformed mean gracility index (GI-MC3) (**C**). Points colour code follows Figure 1. Point size is proportional to mean log CS of each species. On the right, shapes associated with minimum and maximum fitted values (top row) and colour maps of the location and intensity of the shape deformation (bottom row). Blue: minimum value of the regression. Orange: maximum value of the regression. For each bone, the shape associated with the minimum was coloured depending on its distance to the shape associated with the maximum (blue indicates a low deformation intensity and

red indicates a high deformation intensity). Orientation from left to right in each case: caudal, lateral, cranial and medial.

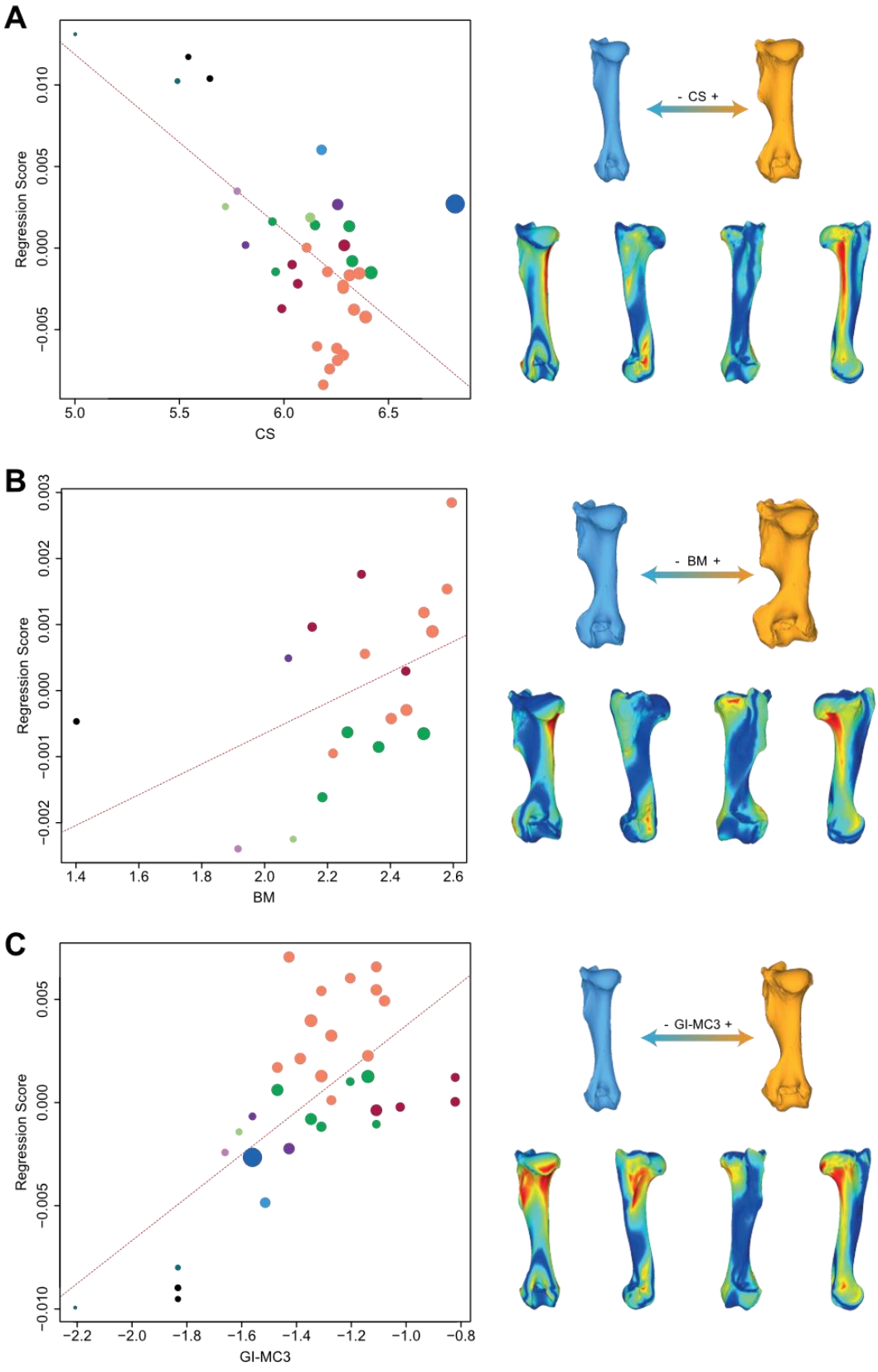

Figure 6. Significant PGLS regression plots for distal partial humerus performed on shape data and log-transformed centroid size (CS) (**A**), log-transformed cubic root of mean body mass (BM) (**B**), log-transformed mean gracility index (GI-MC3) (**C**). Points colour code follows Figure 1. Point size is proportional to mean log CS of each species. On the right, shapes associated with minimum and maximum fitted values (top row) and colour maps of the location and intensity of the shape deformation (bottom row). Blue: minimum value of the regression. Orange: maximum value of the regression. For each bone, the shape associated with the maximum was coloured depending on its distance to the shape associated with the minimum (blue indicates a low deformation intensity and red indicates a high deformation intensity). Orientation from left to right in each case: caudal, lateral, cranial and medial.

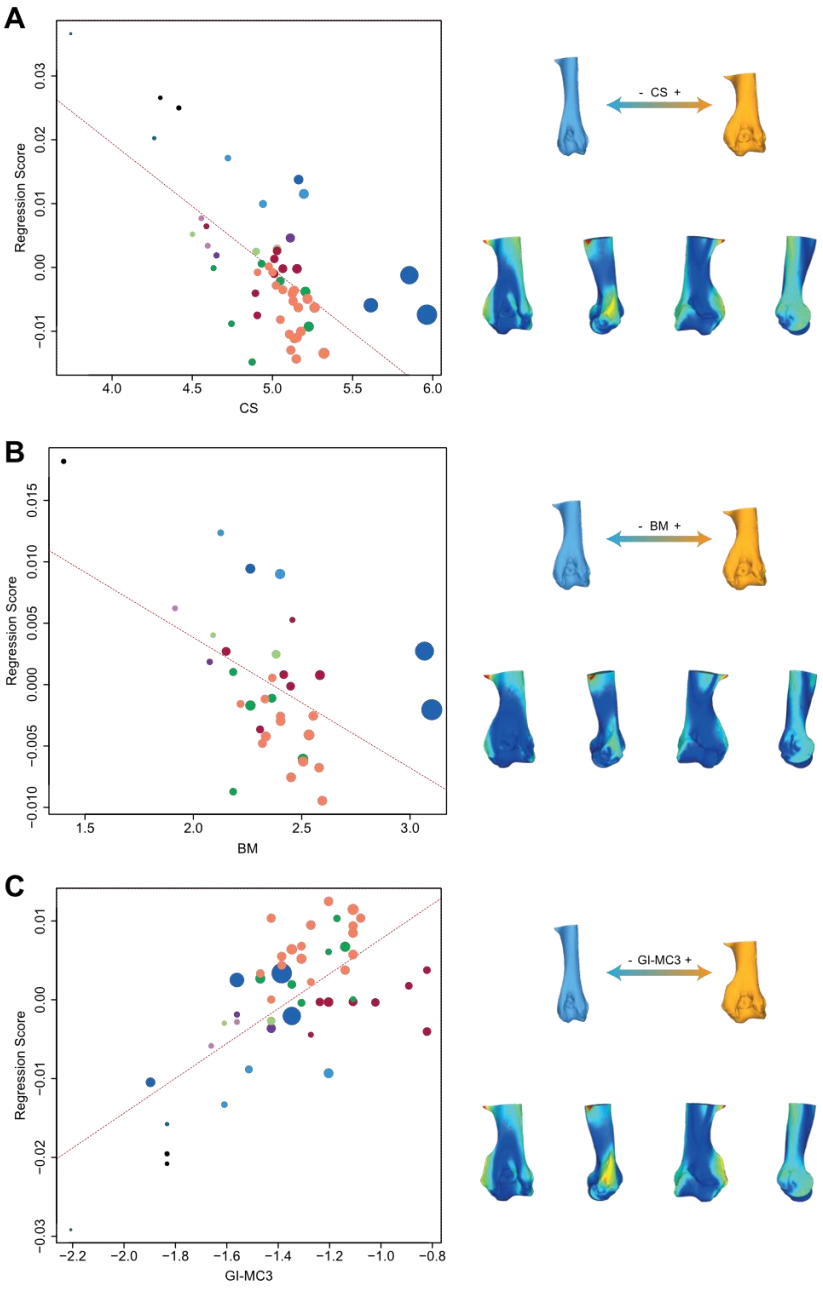

Figure 7. Results of the PCA performed on morphometric data of the radius and shape variation associated with the first axis of the PCA (cranial view). Blue: negative side of the axis. Orange: positive side of the axis. Phylogenetic relationships are plotted in the morphospace. Colour code follows Figure 1 and abbreviations follow Table 1. Point size is proportional to the mean log centroid size of each species.

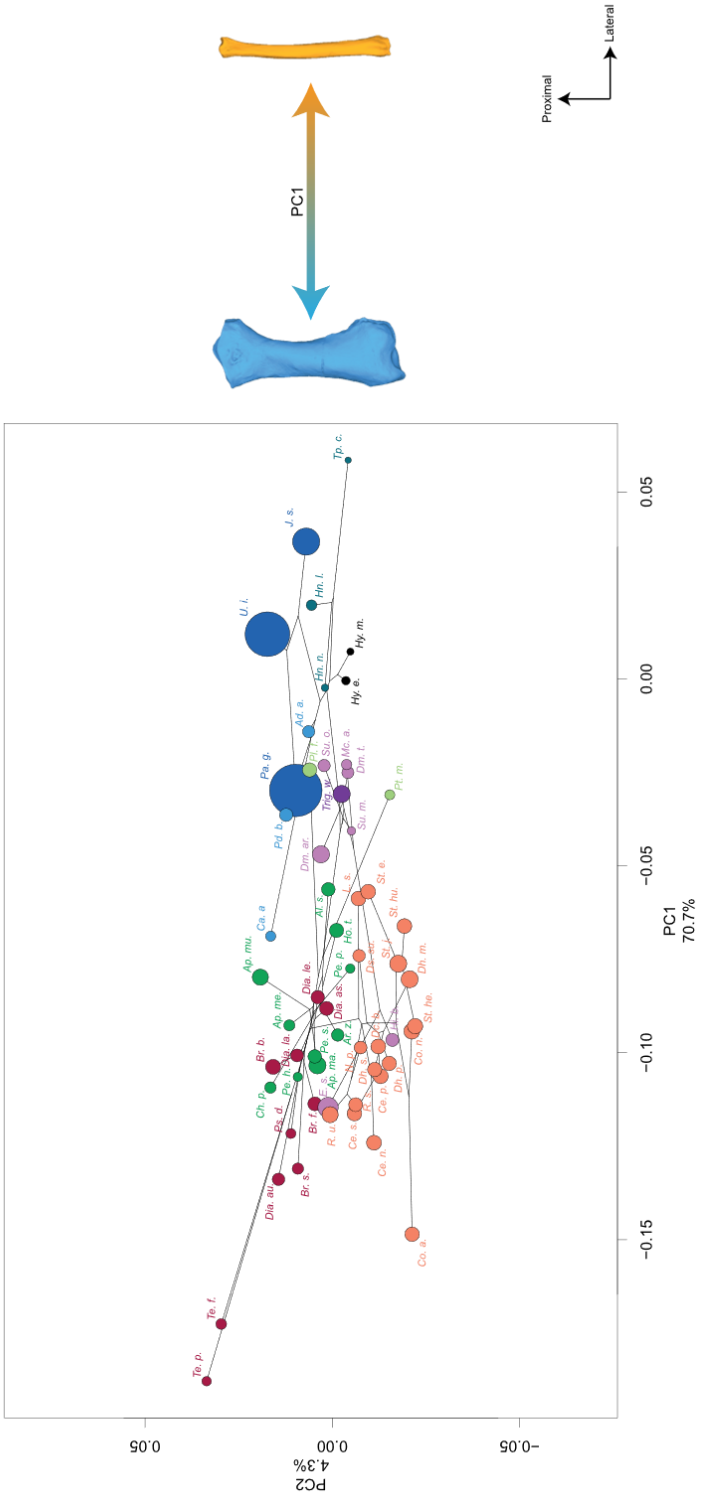

Figure 8. Significant PGLS regression plots for the radius performed on shape data and log-transformed cubic root of mean body mass (BM) (**A**) and log-transformed mean gracility index (GI-MC3) (**B**). Points colour code follows Figure 1. Point size is proportional to mean log CS of each species. On the right, shapes associated with minimum and maximum fitted values (top row) and colour maps of the location and intensity of the shape deformation (bottom row). Blue: minimum value of the regression. Orange: maximum value of the regression. For each bone, the shape associated with the minimum was coloured depending on its distance to the shape associated with the maximum (blue indicates a low deformation intensity and red indicates a high deformation intensity). Orientation from left to right in each case: caudal, lateral, cranial and medial.

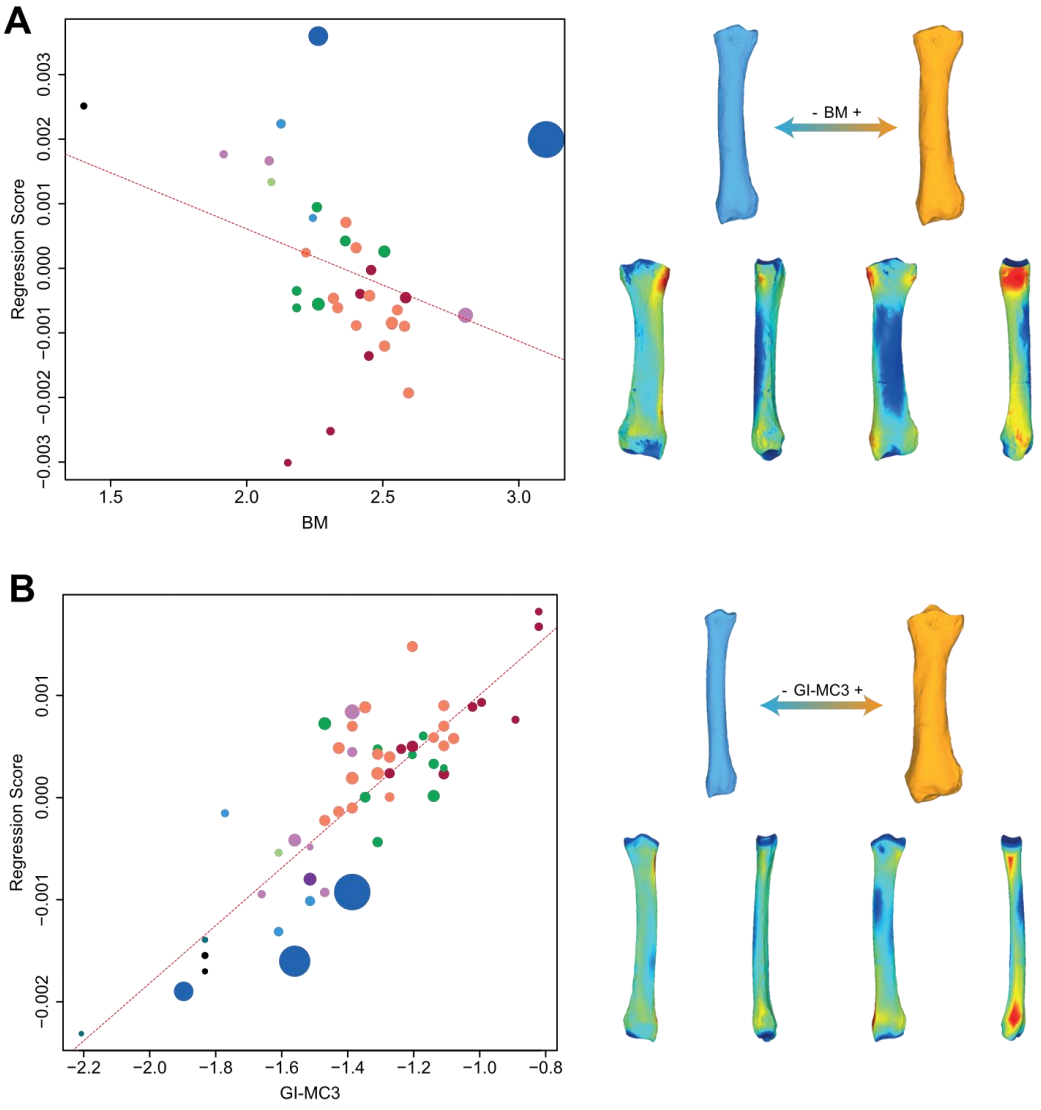

Figure 9. Results of the PCA performed on morphometric data of complete ulna (**A**), ulna without olecranon tuberosity (**B**) and distal partial ulna (**C**) and shape variation associated with the first two axes of the PCA (caudal view). Blue: negative side of the axis. Orange: positive side of the axis.

Phylogenetic relationships are plotted in the morphospace. Colour code follows Figure 1 and abbreviations follow Table 1. Point size is proportional to the mean log centroid size of each species.

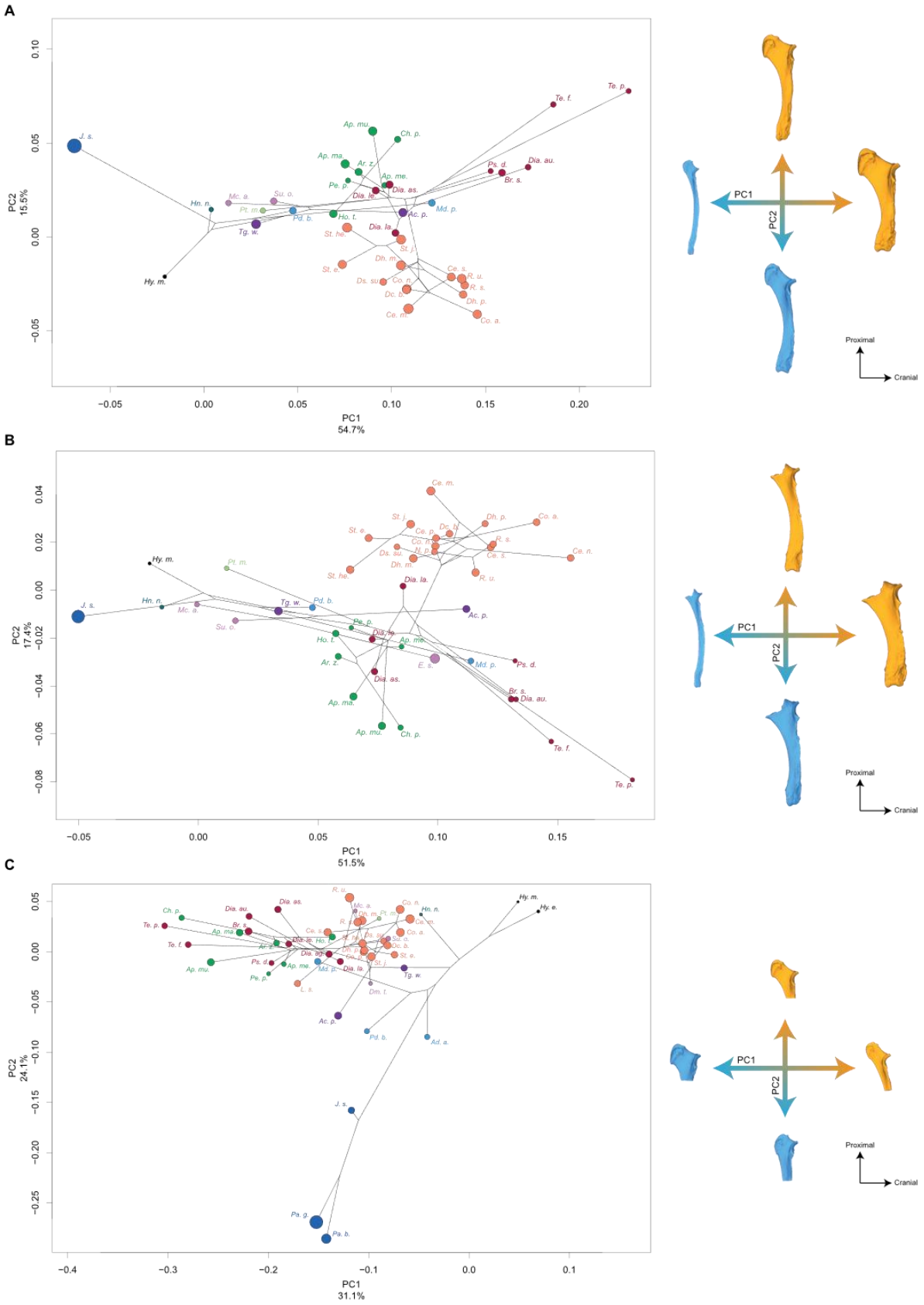

Figure 10. Significant PGLS regression plots for complete ulna (**A**) and ulna without olecranon tuberosity (**B**) performed on shape data and log-transformed mean gracility index (GI-MC3). Points colour code follows Figure 1. Point size is proportional to mean log CS of each species. On the right, shapes associated with minimum and maximum fitted values (top row) and colour maps of the location and intensity of the shape deformation (bottom row). Blue: minimum value of the regression. Orange: maximum value of the regression. For each bone, the shape associated with the minimum was coloured depending on its distance to the shape associated with the maximum (blue indicates a low deformation intensity and red indicates a high deformation intensity). Orientation from left to right in each case: caudal, lateral, cranial and medial.

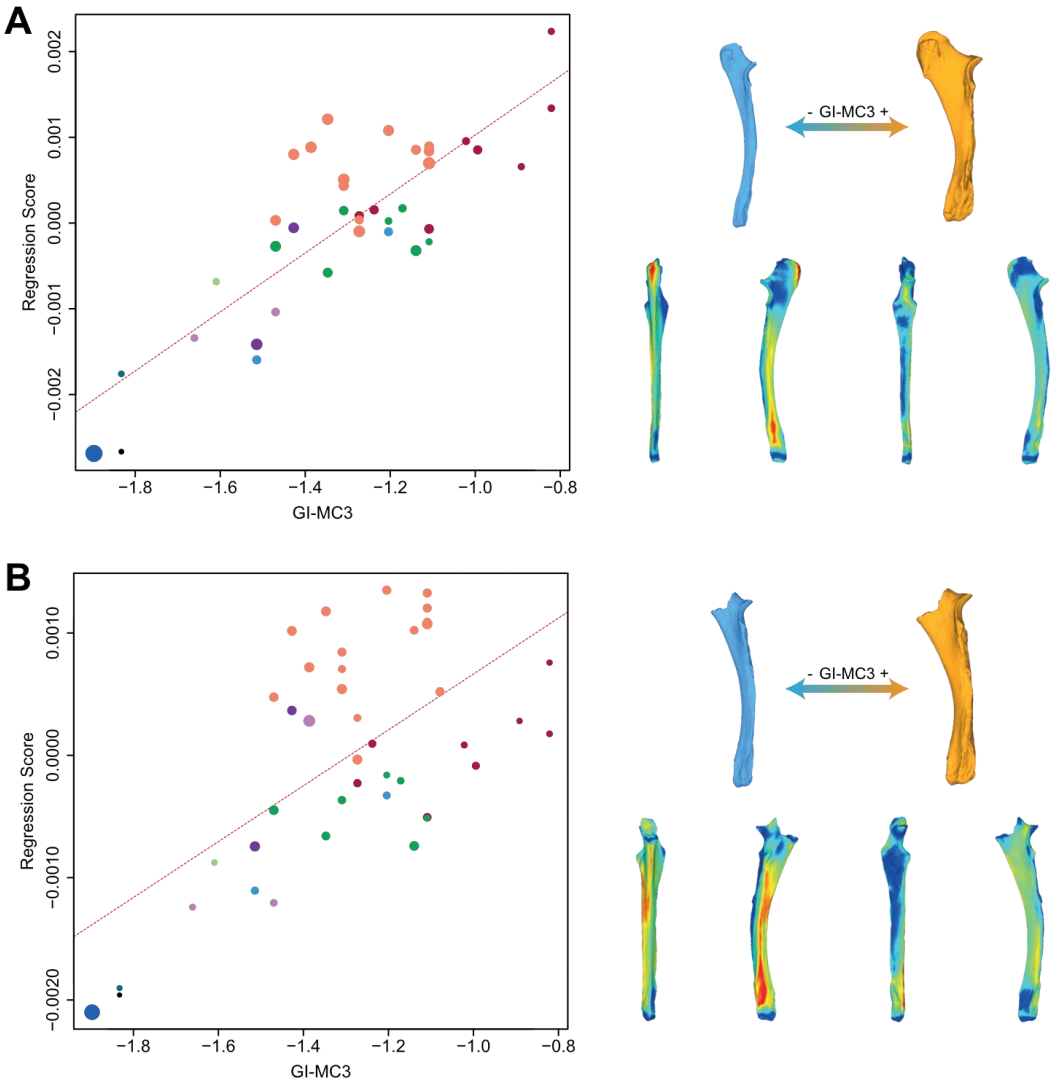

Figure 11. Significant PGLS regression plots for proximal partial ulna performed on shape data and log-transformed centroid size (CS) (**A**), log-transformed cubic root of mean body mass (BM) (**B**), log-transformed mean gracility index (GI-MC3) (**C**). Points colour code follows Figure 1. Point size is proportional to mean log CS of each species. On the right, shapes associated with minimum and

maximum fitted values (top row) and colour maps of the location and intensity of the shape deformation (bottom row). Blue: minimum value of the regression. Orange: maximum value of the regression. For each bone, the shape associated with the minimum was coloured depending on its distance to the shape associated with the maximum (blue indicates a low deformation intensity and red indicates a high deformation intensity). Orientation from left to right in each case: caudal, lateral, cranial and medial.

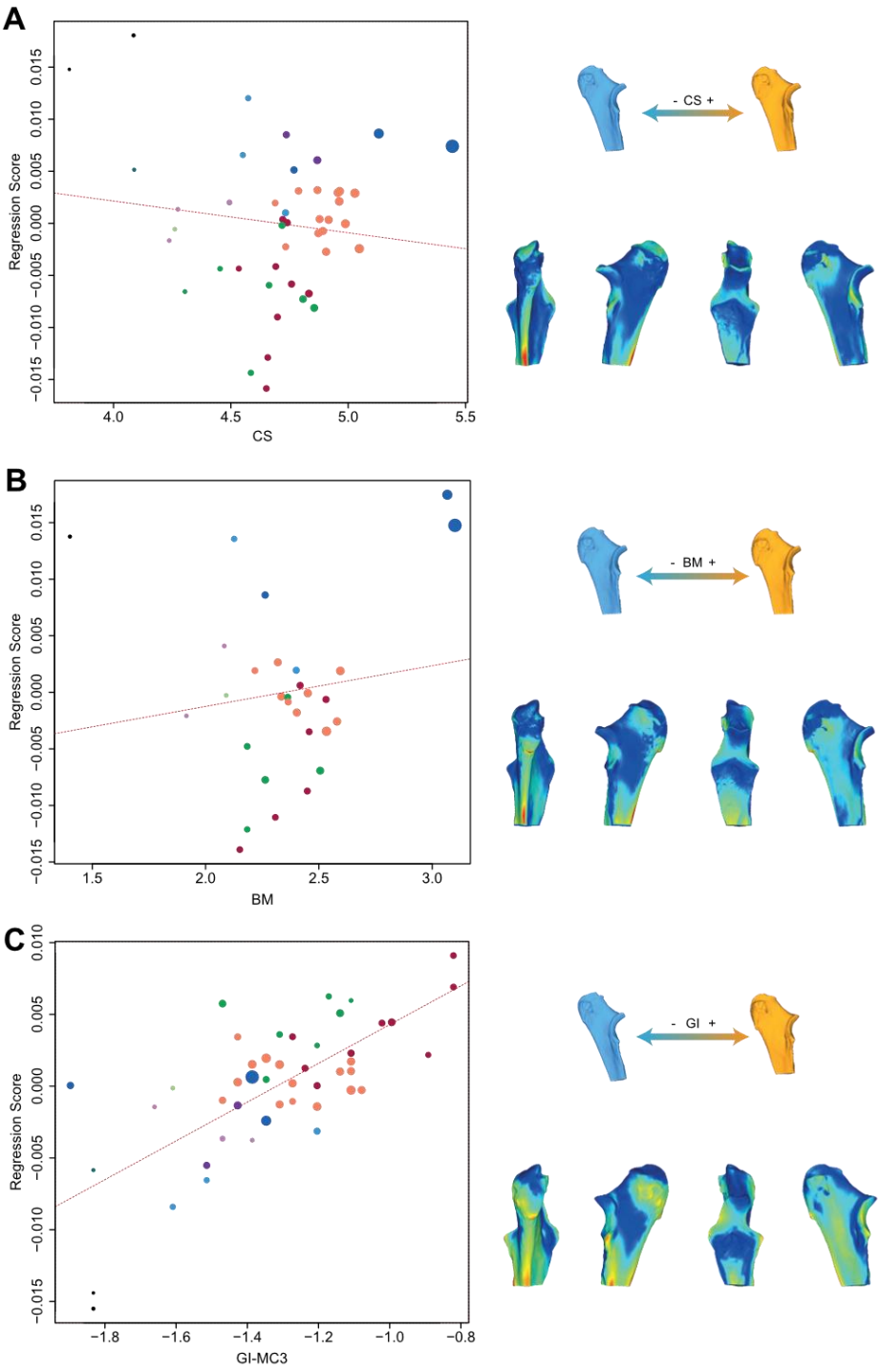

Figure 12. Evolution of centroid size (CS) along the phylogeny for the studied species. **A**: distal partial humerus, **B**: radius, **C**: proximal partial ulna. Computations were made on log-transformed CS. Values at nodes and along branches were reconstructed based on a Brownian motion model of evolution (Revell, 2012). Colour code for taxa follows Figure 1.

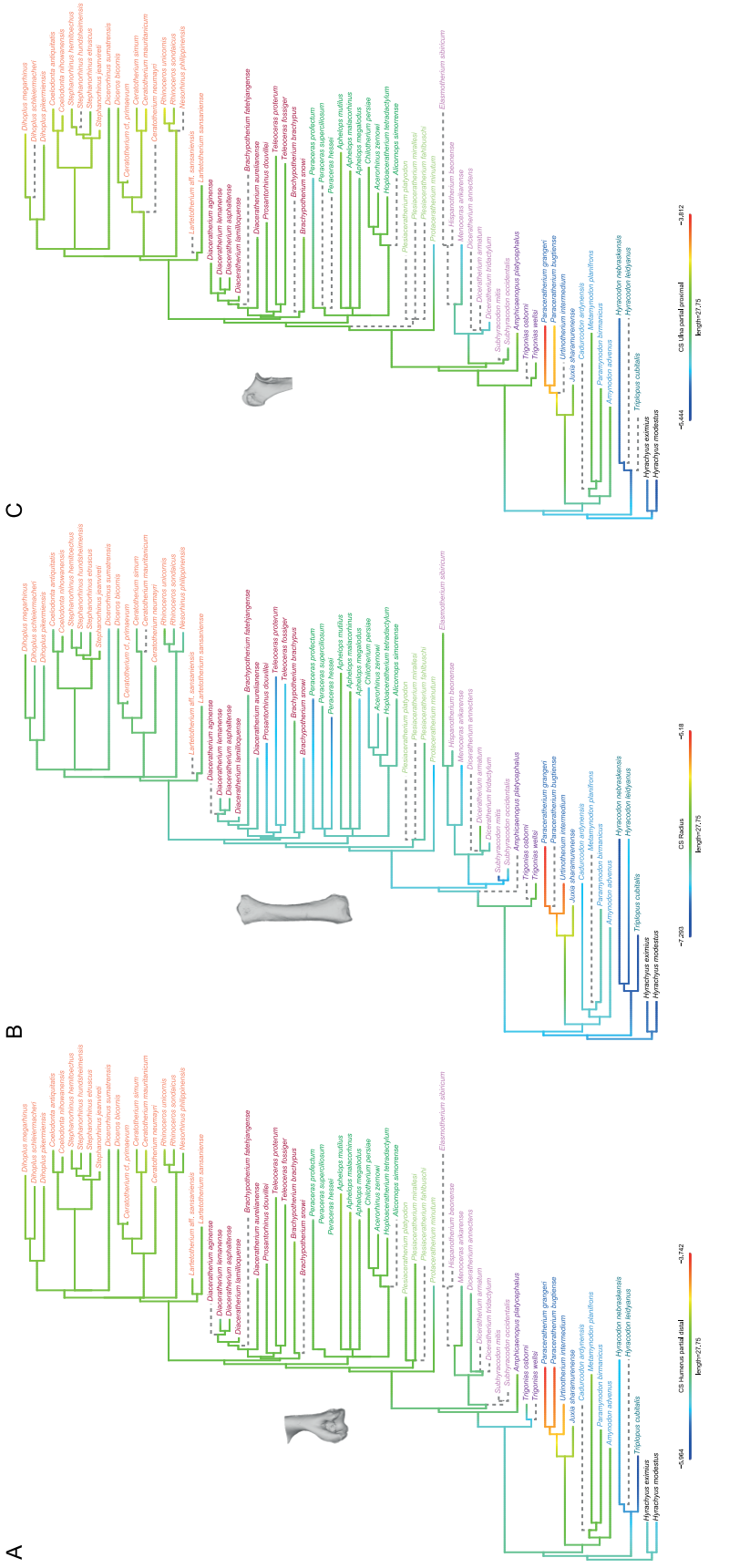
A
B
C
Dinopus megarhinus
Dinopus schleiermacheri
Dinopus pikermensis
Cadurcotherium antiquitatis
Coadiotoma nihowanensis
Stephanorhinus hemitoechus
Stephanorhinus hundsheimensis
Stephanorhinus kirchbergensis
Stephanorhinus jeanvireti
Dicerorhinus sumatrensis
Diceros bicornis
Ceratotherium cf. simum
Ceratotherium simum
Ceratotherium mauritanicum
Ceratotherium neumayri
Rhinoceros unicornis
Rhinoceros sondaicus
Nesorhinus philippinensis
Lartetotherium aff. sansaniense
Lartetotherium sansaniense
Diaceratherium aginense
Diaceratherium asiaticum
Diaceratherium lemanense
Diaceratherium tamiliquense
Brachypotherium fatehjangense
Brachypotherium perimense
Prosantorhinus douvillei
Teleoceras proterum
Teleoceras fossiger
Brachypotherium brachypus
Brachypotherium snowi
Paracoras profectum
Paracoras superciliosum
Persiatherium rarum
Aphelops mutilus
Aphelops malacorhinus
Aphelops megalodus
Chilotherium persiae
Acerorhinus zernowi
Hoploceratherium tetradactylum
Aprotodon africanus
Plesiaceratherium platycodon
Plesiaceratherium mirallesi
Plesiaceratherium fahlbuschi
Protaceratherium minutum
Elasmotherium sibiricum
Hispanotherium beonense
Lartetotherium sansaniense
Diceratherium armatum
Diceratherium annectens
Diceratherium indaclyum
Diceratherium sp.
Subhyracodon occidentalis
Amphicaenopus platycephalus
Trigonias osborni
Trigonias wilsoni
Paracaratherium grangeri
Paracaratherium bugtiense
Urtinotherium intermedium
Juxia sharamurenense
Caduricodon ardynensis
Metamynodon planifrons
Paramynodon benaultus
Amynodon advenus
Hyracodon nebraskensis
Hyracodon leidyanus
Triplopus cubitalis
Hyrachyus eximius
Hyrachyus modestus
CS humerus partial distal
length=21.75
-5.984
-3.742
CS Radius
length=21.75
-7.283
-5.18
CS Ulna partial proximal
length=21.75
-5.444
-3.812

TABLES

Table 1. List of the abbreviations, mean body masses and gracility indexes used in this study, with number of forelimb digits for each species. Sources used to compile mean body mass and gracility index are given in Supplementary Data S4.

Taxon	Abbreviation	Mean body mass (kg)	Gracility Index (McIII)	Number of forelimb digits
Acerorhinus zernowi	Ar. z.	700	0.27	4
Alicornops simorrense	Al. s.	875	0.27	4
Amphicaenopus platycephalus	Ac. p.	NA	0.24	NA
Amynodon advenus	Ad. a.	589	0.20	4
Aphelops malacorhinus	Ap. ma.	889	0.23	4
Aphelops megalodus	Ap. me.	NA	0.30	4
Aphelops mutilus	Ap. mu.	1840	0.32	4
Brachypotherium brachypus	Br. b.	2327	0.30	3
Brachypotherium fatehjangense	Br. f.	1999	NA	3
Brachypotherium snowi	Br. s.	NA	0.37	3
Cadurcodon ardynensis	Ca. a.	837	0.17	4
Ceratotherium cf. *primaevum*	Ce. p.	NA	0.34	3
Ceratotherium mauritanicum	Ce. m.	NA	0.33	3
Ceratotherium neumayri	Ce. n.	1844	0.33	3
Ceratotherium simum	Ce. s.	2300	0.33	3
Chilotherium persiae	Ch. p.	700	0.31	4
Coelodonta antiquitatis	Co. a.	2402	0.30	3
Coelodonta nihowanensis	Co. n.	NA	0.24	3
Diaceratherium aginense	Dia. ag.	1987	0.30	4
Diaceratherium asphaltense	Dia. as.	NA	0.33	4
Diaceratherium aurelianense	Dia. au.	1551	0.36	4
Diaceratherium lamilloquense	Dia. la.	1410	0.29	4
Diaceratherium lemanense	Dia. le.	1590	0.28	4
Diceratherium annectens	Dm. an.	NA	0.21	3
Diceratherium armatum	Dm. ar.	NA	0.21	3
Diceratherium tridactylum	Dm. t.	517	0.25	3
Dicerorhinus sumatrensis	Ds. su.	775	0.28	3
Diceros bicornis	Dc. b.	1050	0.27	3
Dihoplus megarhinus	Dh. m.	NA	0.27	3
Dihoplus pikermiensis	Dh. p.	1100	0.33	3
Dihoplus schleiermacheri	Dh. s.	2123	0.25	3
Elasmotherium sibiricum	E. s.	4500	0.25	3
Hispanotherium beonense	Hi. b.	NA	0.25	3
Hoploaceratherium tetradactylum	Ho. t.	1197	0.26	4
Hyrachyus eximius	Hy. e.	66.6	0.16	4
Hyrachyus modestus	Hy. m.	NA	0.16	4
Hyracodon leidyanus	Hn. l.	NA	NA	3
Hyracodon nebraskensis	Hn. n.	NA	0.16	3
Juxia sharamurenense	J. s.	888	0.15	4
Lartetotherium sansaniense	L. s.	1204	0.24	3
Lartetotherium aff. *sansaniensis*	L. sa.	1232	NA	3
Menoceras arikarense	Mc. a.	313	0.19	3
Metamynodon planifrons	Md. p.	1340	0.30	4
Nesorhinus philippinensis	N. p.	1086	0.27	3
Paraceratherium bugtiense	Pa. b.	9900	0.26	3
Paraceratherium grangeri	Pa. g.	10950	0.25	3
Paramynodon birmanicus	Pd. b.	NA	0.22	4

Peraceras hessei	Pe. h.	NA	NA	4
Peraceras profectum	Pe. p.	NA	0.33	4
Peraceras superciliosum	Pe. s.	NA	0.32	4
Plesiaceratherium fahlbuschi	Pl. f.	NA	NA	4
Plesiaceratherium mirallesi	Pl. m.	1268	0.24	4
Plesiaceratherium platyodon	Pl. p.	NA	NA	4
Prosantorhinus douvillei	Ps. d.	NA	0.41	3
Protaceratherium minutum	Pt. m.	530	0.20	4
Rhinoceros sondaicus	R. s.	1350	0.32	3
Rhinoceros unicornis	R. u.	2000	0.26	3
Stephanorhinus jeanvireti	St. j.	NA	0.25	3
Stephanorhinus etruscus	St. e.	NA	0.23	3
Stephanorhinus hemitoechus	St. he.	1561	0.28	3
Stephanorhinus hundsheimensis	St. hu.	1348	0.25	3
Subhyracodon mitis	Su. m.	NA	0.22	3
Subhyracodon occidentalis	Su. o.	NA	0.23	3
Teleoceras fossiger	Te. f.	1016	0.44	3
Teleoceras proterum	Te. p.	635	0.44	3
Trigonias osborni	Tg. o.	506	0.21	4
Trigonias wellsi	Tg. w.	NA	0.22	4
Triplopus cubitalis	Tp. c.	NA	0.11	3
Urtinotherium intermedium	U. i.	NA	0.21	3

1330

1331 **Table 2.** Results of the Pearson's correlation tests between centroid size (CS), and mean body mass
1332 (BM) and mean gracility index (GI-MC3) respectively for each bone (computed on Phylogenetic
1333 Independent Contrasts). **r:** Pearson's correlation coefficient value; **t:** student distribution value; **dF:**
1334 degrees of freedom; **p**: p-value. Significant results (for $p < 0.01$) are indicated in bold.

Bone	Variables	r	t	dF	p
Humerus (complete)	**CS ~ BM**	**0.64**	**3.32**	**16**	**< 0.01**
	CS ~ GI-MC3	0.37	2.16	30	0.03
Humerus (distal partial)	**CS ~ BM**	**0.72**	**5.87**	**31**	**< 0.01**
	CS ~ GI-MC3	**0.50**	**3.91**	**47**	**< 0.01**
Radius	**CS ~ BM**	**0.80**	**7.48**	**32**	**< 0.01**
	CS ~ GI-MC3	0.06	0.41	51	0.68
Ulna (complete)	CS ~ BM	0.44	2.16	19	0.04
	CS ~ GI-MC3	-0.12	-0.73	35	0.47
Ulna (without ol. tub.)	**CS ~ BM**	**0.52**	**2.84**	**22**	**< 0.01**
	CS ~ GI-MC3	-0.13	-0.82	39	0.41
Ulna (proximal partial)	**CS ~ BM**	**0.85**	**8.40**	**26**	**< 0.01**
	CS ~ GI-MC3	0.28	1.92	43	0.06

1335

1336

Table 3. Range of R^2 and p-values for PGLS computed with NNI permuted trees on shape data and log-transformed centroid size (CS), log-transformed cubic root of mean body mass (BM) and log-transformed mean gracility index (GI-MC3). **N:** number of trees obtained after NNI procedure; **R^2:** determination coefficient value. Significant results (for $p < 0.01$) are indicated in bold.

Bone	**Variable**	**N**	**R^2**			**p-value**		
			Min.	**Max.**	**Mean**	**Min.**	**Max.**	**Mean**
Humerus (complete)	**CS**	**66**	**0.09**	**0.12**	**0.11**	**0.001**	**0.006**	**0.002**
	BM	**34**	**0.19**	**0.40**	**0.22**	**0.001**	**0.002**	**0.001**
	GI-MC3	**62**	**0.10**	**0.17**	**0.12**	**0.001**	**0.002**	**0.001**
Humerus (distal partial)	**CS**	**102**	**0.20**	**0.28**	**0.22**	**0.001**	**0.001**	**0.001**
	BM	**63**	**0.19**	**0.26**	**0.20**	**0.001**	**0.001**	**0.001**
	GI-MC3	**96**	**0.14**	**0.24**	**0.21**	**0.001**	**0.001**	**0.001**
Radius	CS	114	0.02	0.03	0.02	0.083	0.306	0.226
	BM	**65**	**0.05**	**0.16**	**0.11**	**0.001**	**0.173**	**0.009**
	GI-MC3	**104**	**0.17**	**0.22**	**0.20**	**0.001**	**0.002**	**0.001**
Ulna (complete)	CS	72	0.02	0.04	0.03	0.203	0.615	0.382
	BM	40	0.05	0.08	0.07	0.111	0.303	0.205
	GI-MC3	**72**	**0.20**	**0.26**	**0.23**	**0.001**	**0.001**	**0.001**
Ulna (without ol. tub.)	CS	80	0.02	0.03	0.02	0.268	0.741	0.661
	BM	45	0.09	0.11	0.10	0.030	0.068	0.046
	GI-MC3	**80**	**0.18**	**0.22**	**0.20**	**0.001**	**0.001**	**0.001**
Ulna (proximal partial)	**CS**	**88**	**0.06**	**0.13**	**0.08**	**0.001**	**0.008**	**0.002**
	BM	**54**	**0.12**	**0.23**	**0.15**	**0.001**	**0.006**	**0.005**
	GI-MC3	**88**	**0.06**	**0.09**	**0.08**	**0.001**	**0.007**	**0.002**

SUPPORTING INFORMATION

Table S1: Complete list of all the studied specimens.

Figure S2: Summary of the anatomical areas of the rhino long bone. Bones figured here belong to *C. simum*. **A: Humerus. Abbreviations** – B.g.: Bicipital groove; C.: Capitulum; D.t.: Deltoid tuberosity; E.c.: Epicondylar crest; G.t.: Greater tubercle; G.t.c.: Greater tubercle convexity; H.: Head; I.t.: Intermediate tubercle; L.e.: Lateral epicondyle; L.l.b.: Lateral lip border; L.t.: Lesser tubercle; L.t.c.: Lesser tubercle convexity; M.e.: Medial epicondyle; M.i.i.: M. infraspinatus insertion; M.l.b.: Medial lip border; M.t.m.t.: M. teres major tuberosity; N.: Neck; O.f.: Olecranon fossa; T.: Trochlea; T.g.: Trochlear groove. **B: Radius. Abbreviations** – A.s.s.: Articular surface for the scaphoid; A.s.sl.: Articular surface for the semilunar; C.p.: Coronoid process; D.a.s.u.: Distal articular surface for the ulna; I.c.: Interosseous crest; I.s.: Interosseous space; L.g.c.: Lateral glenoid cavity; L.i.r.: Lateral insertion relief; L.s.a.s.: Lateral synovial articular surface; M.g.c.: Medial glenoid cavity; M.s.a.s.: Medial synovial articular surface; P.a.s.u.: Proximal articular surface for the ulna; P.p.: Palmar process; R.s.p.: Radial styloid process; R.t.: Radial tuberosity. **C: Ulna. Abbreviations** – A.p.: Anconeal process; A.s.h.: Articular surface for the humerus; A.s.p.: Articular surface for the pisiform; A.s.sl.: Articular surface for the semilunar; A.s.t.: Articular surface for the triquetrum; D.a.s.r.: Distal articular surface for the radius; I.c.: Interosseous crest; I.s.: Interosseous space; M.t.o.: Medial tuberosity of the olecranon; O.t.: Olecranon tuberosity; P.b.: palmar border; U.s.p.: Ulnar styloid process.

Data S3: Designation and location of the anatomical landmarks placed on each bone.

Data S4: Complete list of gracility index and mean body mass compiled from literature.

Table S5: Summary of the differences in p and R^2 values between the PGLS computed under a Brownian Motion (BM) model (geomorph) and a Ridge Regression (RR) model (RRphylo). Only variables with significant results are presented here.

Figure S6: Shape deformations associated with the first two axes of the PCA for each bone. Blue: minimal values. Orange: maximal values. Orientation from left to right: caudal, lateral, cranial, medial, proximal and distal views. **A:** complete humerus; **B**: distal partial humerus; **C:** radius; **D:** complete ulna; **E**: ulna without olecranon tuberosity; **F:** proximal partial ulna.

Figure S7: Shape deformations associated with minimum and maximum values of the centroid size (CS), body mass (BM) and gracility index (GI-MC3) for significant regressions with shape. Blue: minimal values. Orange: maximal values. Orientation from left to right: caudal, lateral, cranial, medial, proximal and distal views. **A, B, C:** complete humerus; **D, E, F**: distal partial humerus; **G, H:** radius; **I:** complete ulna; **J**: ulna without olecranon tuberosity; **K, L, M:** proximal partial ulna.

Figure S8. Significant PGLS regression plots ulna without olecranon performed on shape data and log-transformed cubic root of mean body mass (BM). Points colour code follows Figure 1. Point size is proportional to mean log CS of each species. On the right, shapes associated with minimum and maximum fitted values (top row) and colour maps of the location and intensity of the shape deformation (bottom row). Blue: minimal values. Orange: maximal values. For each bone, the shape associated with the minimum was coloured depending on its distance to the shape associated with the maximum (blue indicates a low deformation intensity and red indicates a high deformation intensity). Orientation from left to right in each case: caudal, lateral, cranial and medial views.

Figure S9. Number of digits for each species plotted on the Neighbour Joining trees computed on all PC scores as in Figure 3. Colour code of species names follows Figure 1 and abbreviations follow Table 1. Colour code for number of digits as indicated on the bottom of the figure. Point size is proportional to the mean log centroid size of each species. **A:** complete humerus; **B**: distal partial humerus; **C:** radius; **D:** complete ulna; **E**: ulna without olecranon tuberosity; **F:** proximal partial ulna.